Lithos 378–379 (2020) 105805

Contents lists available at ScienceDirect

Lithos

journal homepage: www.elsevier.com/locate/lithos

Research Article

A ~2.051 Ga anatectic event and peraluminous leucogranite from the Mahalapye Complex, northern edge of the Kaapvaal Craton: Record of an effect of Bushveld mafic magmatism

H.M. Rajesh [a,*], O.G. Safonov [b,c,d], G.A. Belyanin [d], C. Vorster [d,e]

[a] Department of Earth and Environmental Sciences, BIUST, Botswana
[b] Korzhinskii Institute of Experimental Mineralogy RAS, Chernogolovka, Russia
[c] Department of Petrology and Volcanology, Geological Faculty, Moscow State University, Russia
[d] Department of Geology, University of Johannesburg, South Africa
[e] DST-NRF Centre of Excellence for Integrated Mineral and Energy Resource Analysis (CIMERA), University of Johannesburg, South Africa

ARTICLE INFO

Article history:
Received 29 April 2020
Received in revised form 28 September 2020
Accepted 28 September 2020
Available online 01 October 2020

Keywords:
Garnet-bearing diorite gneiss
Peraluminous leucogranite
Mahalapye complex high-grade terrane
Paleoproterozoic Bushveld LIP
Kaapvaal Craton

ABSTRACT

Anatectic events and related leucogranites are rarely reported from Precambrian large igneous provinces (LIPs). However, their appearance is possible in relation to the intrusion of later pulses of mafic magmas into the earlier rocks. Silicic intrusive rocks associated with the ~2.06–2.05 Ga Bushveld LIP within the Kaapvaal Craton include granites, syenites or granophyres. This study reports *syn*-Bushveld partial melting of ~2.061 Ga diorite gneiss producing leucogranite from the Mahalapye Complex high-grade terrane, at the northern edge of the Kaapvaal Craton. Both the migmatitic diorite gneiss and associated leucogranite are crosscut by the ~2.039 Ga granodiorite. The different stages of melting of the biotite-bearing diorite gneiss – from onset of melting to melt segregation – are well preserved. Petrographic continuity between the leucosomes, and concordant and discordant leucogranite bodies point to a melt flow-accumulation network. Garnet formed after biotite during partial melting. Phase equilibria modelling and conventional thermobarometry indicate conditions of ~730 °C and ~7.2–7.5-kbar for the anatectic event. The predicted melt composition is peraluminous, magnesian and alkali-calcic, that is comparable to the chemistry of leucogranites. The low content of anatectic melt for the estimated P-T condition corresponds to the occurrence of leucogranites as thin veins to dykes. LA-MC-ICPMS U–Pb zircon age of 2051.3 ± 6.8 Ma is interpreted to date the anatectic event. The leucogranite exhibits co-mingling structures with dyke-like and sill-like *syn*-Bushveld norite intrusions associated with diorite gneiss. Preferential accumulation of the leucocratic material along the contact of diorite gneiss and norite, and the liquid-liquid interface with the norite, indicate the close age of leucogranite and norite. This is supported by the LA-Q-ICPMS U–Pb zircon age of 2054 ± 7.9 Ma from the norite. Thus, the partial melting of the diorite gneiss and formation of the leucogranites is argued as a response to Bushveld mafic magmatism. The present study shows that one of the causative agents of overprint event(s) in high-grade terranes along Archean cratonic margins can be mafic magmatism of similar age within the craton. However, in the case of LIP-related magmatism the footprints are restricted to terranes immediately adjacent to the cratonic margins.

1. Introduction

Precambrian large igneous provinces (LIPs) typically include volcanics, dykes, sills, layered ultramafic-mafic intrusions, and silicic-carbonatitic rocks (Ernst, 2014). The silicic intrusive rocks are represented by granites, especially alkaline varieties, and syenites, as a part of alkaline complexes. They can form throughout the whole period of evolution of a particular LIP. For example, the silicic intrusive rocks related to the ~2.06–2.05 Ga Bushveld LIP in the Kaapvaal Craton include granites, syenites and granophyres of the 2.060–2.051 Ga Schiel Complex, the ~2.057–2.055 Ga Okwa Complex, ~2.055–2.053 Ga Rashoop granophyre suite, ~2.054 Ga Lebowa granite suite, ~2.054 Ga Moshaneng and Segwagwa-Masoke complexes, and the ~2.052 Ga Schurwedraai Complex (Figs. 1 and 2; see Rajesh et al., 2013a and references therein for details; Ernst, 2014).

Peraluminous leucogranites are rare in Precambrian LIPs. This type of granitoid is commonly generated due to remelting of supracrustal protoliths (Jung et al., 2000; Montel and Vielzeuf, 1997; Patiño Douce, 1999). Hence, there is a possibility for anatexis of earlier formed rocks by later pulses of mafic magmas and formation of leucogranite as part of LIPs. In fact, migmatites related to thermal metamorphism are

* Corresponding author.
E-mail address: rajesh.hm@biust.ac.bw (H.M. Rajesh).

https://doi.org/10.1016/j.lithos.2020.105805

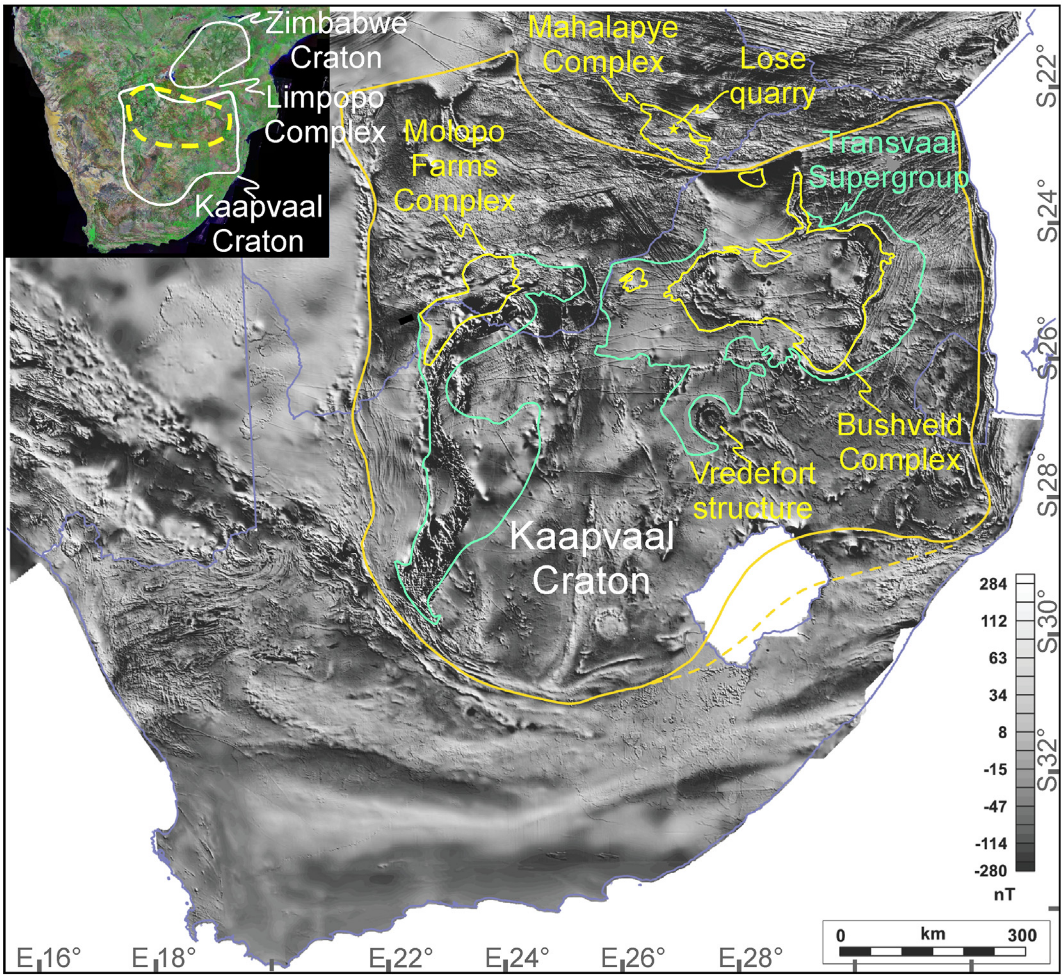

Fig. 1. The known extent of Kaapvaal Craton (yellow line; allochthonous zone is dashed) shown on a total magnetic intensity (TMI) image of southern Africa (reproduced and modified after McCarthy et al., 2018). The Bushveld Complex and Molopo Farms Complex layered intrusions, Transvaal Supergroup, Vredefort structure, and the Mahalapye Complex high-grade terrane are indicated. Inset is a satellite image of southern Africa showing the approximate extent of the Archean Kaapvaal and Zimbabwe cratons. The region between the southern margin of the Zimbabwe Craton and the northeastern margin of the Kaapvaal Craton constitute the Limpopo Complex high-grade terrane. The low seismic velocity cratonic mantle zone at 150 km depth that is related to the massive Bushveld magmatic event is shown as a yellow dotted line [from James and Fouch, 2002]. (For interpretation of the references to colour in this figure legend, the reader is referred to the web version of this article.)

commonly reported along the contact aureoles of layered ultramafic-mafic intrusions associated with LIPs. An example is the migmatites from the eastern contact aureole of the Bushveld Complex layered intrusion (Fig. 1; Harris et al., 2003; Johnson et al., 2003). However, it is unclear whether the melts derived in wall-rocks are able to migrate from the protolith to form separate leucogranite bodies.

This paper describes leucogranites from the Mahalapye Complex, at the northern edge of the Kaapvaal Craton. The study is aimed to test the idea that the anatectic event, producing these leucogranites by melting of diorite gneiss, is related to Bushveld mafic magmatism and, thus, the leucogranite belongs to the Bushveld LIP. The results are important for understanding the causative agent of overprint event(s) in Archean high-grade terranes along cratonic margins.

2. Geological setting

2.1. Bushveld LIP

The ~2.06–2.05 Ga Bushveld LIP consists of a variety of coeval magmatic rocks widely distributed within the central to northwestern Kaapvaal Craton (Figs. 1 and 2; Rajesh et al., 2013a and references therein; Ernst, 2014). Two prominent units of this LIP are the ~2.056–2.054 Ga Bushveld Complex and Molopo Farms Complex layered intrusions (Fig. 1; Scoates and Friedman, 2008, Scoates et al., 2012; Maier et al., 2013; Zeh et al., 2015; Mungall et al., 2016; Kaavera et al., 2018; Beukes et al., 2019). Other smaller intrusions of similar age occur within the Kaapvaal Craton (Fig. 2). A summary of the various intermediate and silicic rocks associated with the Bushveld LIP is given in Table 1.

Migmatitic rocks occur along the contact aureole of the Bushveld Complex layered intrusion with the surrounding Transvaal Supergroup sediments (Fig. 1; Nell, 1985; Engelbrecht, 1990; Kaneko and Miyano, 1990; Waters and Lovegrove, 2002;Harris et al., 2003 ; Johnson et al., 2003). Biotite and muscovite-bearing leucosomes, granitic veins (~2–10 cm wide), and granite sheets (maximum width: ~50 cm) are associated with the migmatite zone in the eastern contact aureole of the Bushveld Complex (Harris et al., 2003; Johnson et al., 2003). They are considered as products of fluid-enhanced melting of the underlying biotite-rich pelitic/psammitic sediments (Harris et al., 2003). Leucosomes usually contain peritectic garnet indicating melting at low water activity (Johnson et al., 2003). The extent of melting was highly heterogeneous, with the overall leucosome fractions <5 vol%. Temperatures of 750 ± 50 °C at pressures 2–5 kbar were estimated for the migmatite zone along the aureole (Engelbrecht, 1990; Harris et al.,

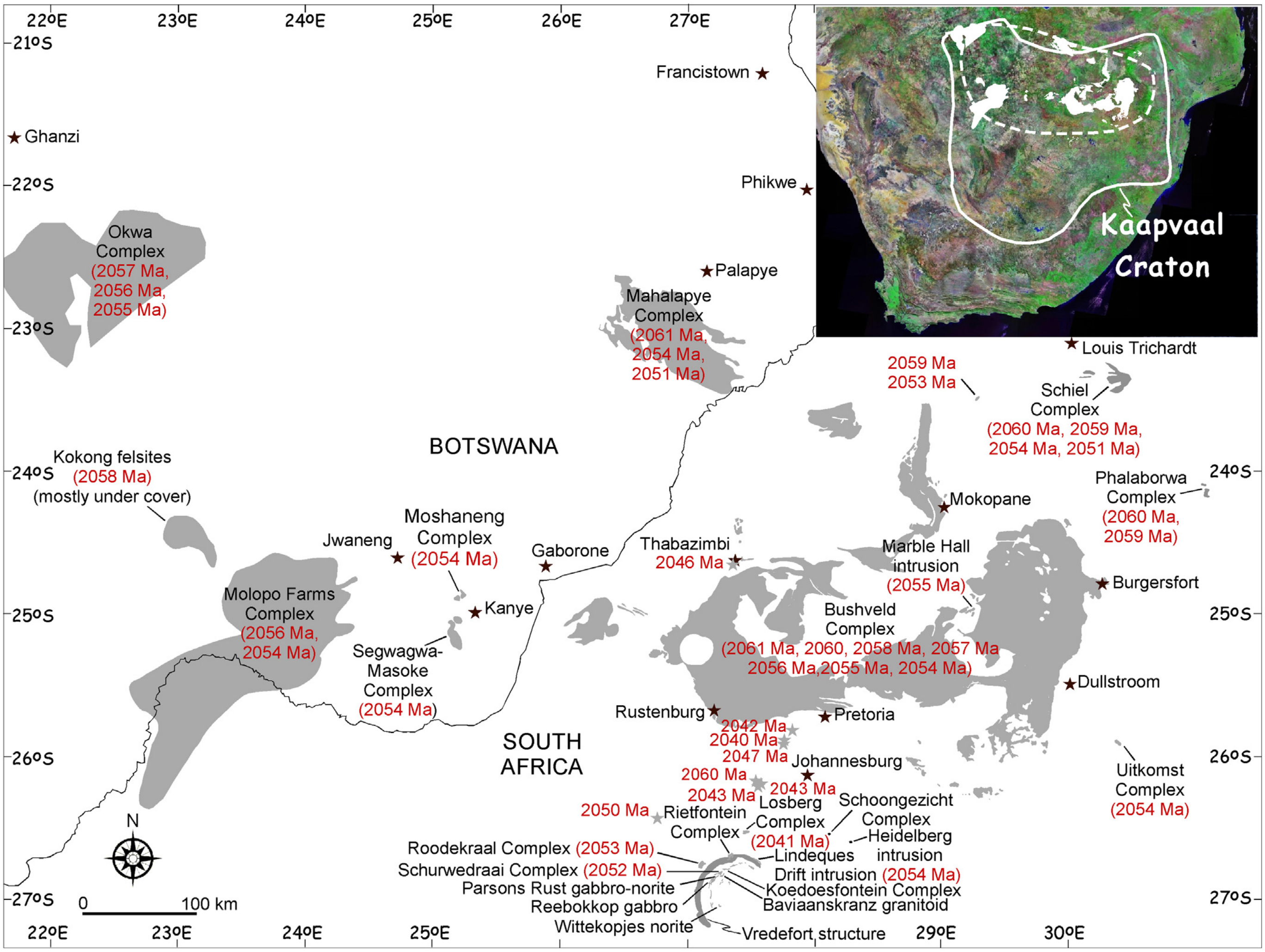

Fig. 2. Geological map of southern Africa showing the distribution of different *syn*-Bushveld units constituting the Bushveld LIP (modified from Rajesh et al., 2013a). Available geochronological data from each unit is indicated in red. Source for geochronologic data include references compiled in Rajesh et al. (2013a), with additions from Laurent and Zeh (2015), Huthmann et al. (2016), Wabo et al. (2016), Graupner et al. (2018), and Beukes et al. (2019). The Rashoop granophyre suite and Lebowa granite suite forms part of the Bushveld Complex, and are not separately highlighted. The dotted line in the inset is the same as in Fig. 1. (For interpretation of the references to colour in this figure legend, the reader is referred to the web version of this article.)

2003; Johnson et al., 2003; Kaneko and Miyano, 1990; Nell, 1985; Waters and Lovegrove, 2002).

2.2. Mahalapye Complex

The Mahalapye Complex is a granitoid-migmatitic gneiss terrane at the northern edge of the Kaapvaal Craton (Fig. 1; Skinner, 1978; Key, 1979; Ermanovics, 1980; Carney et al., 1994; Chavagnac et al., 2001; McCourt and Armstrong, 1998; Holzer et al., 1999; McCourt et al., 2004; Hisada et al., 2000, 2005; Zeh et al., 2007; Millonig et al., 2010; Rajesh, 2019). It is a part of the Limpopo Complex, an amphibolite- to granulite-facies metamorphic terrane located between the southern margin of the Archean Zimbabwe Craton and the northeastern margin of the Archean Kaapvaal Craton (Fig. 3). The margins of the Mahalapye Complex are delineated by the Sunnyside shear zone to the north, and the Mahalapye shear zone to the south (Fig. 3; Holzer et al., 1999; McCourt et al., 2004). The mapped extent of the migmatitic gneisses define the eastern limit, while the northwestern and western limits of the complex are hidden by cover rocks (Fig. 3).

The 2060.9 ± 6.3 Ma (U–Pb zircon; Zeh et al., 2007) diorite gneisses are the oldest rocks within the Mahalapye Complex. They are followed by a series of leucogranites, granodiorites and alkali granites. Available geochronologic data indicate the following ages for these granitoids: 2045 ± 8 Ma (U–Pb monazite; Millonig et al., 2010) for the leucogranites, 2039 ± 9 Ma and 2037 ± 12 Ma (U–Pb zircon; Millonig et al., 2010) are reported for the granodiorites, and ~ 2.02 Ga [2023 ± 11 Ma; 2023 ± 7 Ma, 2026 ± 10 Ma (U–Pb zircon); McCourt and Armstrong, 1998; Zeh et al., 2007] for the alkali granites. Amphibolites and metapelites occur as xenoliths within the granitoid bodies (Fig. 3). In addition, Rajesh (2019) reported ~2.05 Ga dyke-like and sill-like norite intrusions from the Lose quarry within the Mahalapye Complex. Both the diorite gneiss and norite are considered as part of the Bushveld LIP (Fig. 2; Rajesh et al., 2013a; Ernst, 2014; Rajesh, 2019).

3. Field relations

In contrast to previous studies which lumped the leucogranites in the Mahalapye Complex as a single unit, we distinguish two types of leucogranites (referred here as leucogranite 1 and 2) with respect to their relation to the ~2.04 Ga granodiorite. The dominant leucogranite 2, which are best exposed in central and eastern parts of the Mahalapye Complex, forms massive bodies that crosscut the granodiorite. They

Table 1
Summary of intermediate and silicic rock types, available ages and related geologic units of the Bushveld LIP.

Geologic unit	Intermediate and silicic rock type(s)	Age (Ma)*
Schiel complex	Syenite, Quartz syenite, Granite	2060 ± 4; 2059 ± 35; 2054 ± 4; 2051 ± 6; 2050 ± 10
Okwa complex	Granite, Microgranite, Augen gneiss	2057 ± 2; 2056 ± 1; 2055 ± 1
Rashoop granophyre suite (Bushveld Complex)	Granophyre, Granite porphyry	2055.7 ± 1; 2053 ± 12
Marble Hall intrusion	Diorite, Meladiorite, Leucodiorite	2055.6 ± 3.1
Lindeques Drift intrusion	Diorite, Leucodiorite, Syenodiorite	2054.8 ± 5.7
Lebowa granite suite (Bushveld Complex)	Alkali granite, Microgranite	2054.2 ± 3.5; 2054 ± 2
Moshaneng Complex	Diorite, Syenite, Porphyritic granite	2054 ± 2
Segwagwa-Masoke Complex	Diorite, Granite, Syenite	2054 ± 9
Roodekraal Complex	Diorite	2053 ± 9.2
Schurwedraai Complex	Alkali granite, Nepheline syenite	2052 ± 14

* U-Pb zircon ages; see Rajesh et al. (2013a) for references on the age data, with additions from Laurent and Zeh (2015) and Graupner et al. (2018).

contain large enclaves of diorite gneiss, granodiorite and metapelite. The less dominant leucogranite 1 forms thin veins to dykes associated with diorite gneiss and are crosscut by the granodiorite. The present study deals with the formation and timing of leucogranite 1 (leucogranite hereafter). It is argued that leucogranite 1 is related to the Bushveld LIP, while the leucogranite 2 is not.

The mutual relationships between the leucogranite and associated diorite gneiss, norite, and granodiorite are well exposed at the Lose quarry (Fig. 3). Diorite gneiss occurs as porphyritic and non-porphyritic varieties (Fig. 4a). They are migmatitic with crisscrossing leucosome veins, which are locally outlined by biotite-rich margins (Fig. 4b). Both layer-parallel, as well as cross-cutting leucosomes, occur (Fig. 4c). Garnet is locally present in the diorite gneiss and is widely distributed as separate grains and aggregates in the leucosomes (Fig. 4d). With melt segregation, asymmetric structures including intrafolial-, ptygmatic-folds, and boudinage develop (Figs. 4e, f). As the degree of partial melting increases, leucosomes start to form leucogranite veins with irregular margins (Fig. 4g). In turn, the veins join to form leucogranite dykes with less irregular to near-straight line margins (Figs. 4g, h). The leucosomes and leucogranite show petrographic continuity on different scales (Fig. 4 g, h). Garnet size decreases from leucosome to leucogranite. Dismembered fragments of leucosome occur within the granodiorite (Figs. 4a and 5a). In comparison to those associated with diorite gneiss, leucosomes within granodiorite have less irregular outlines and no biotite-rich margins.

Linear dyke-like and sill-like norite bodies are associated with diorite gneiss and leucogranite (Figs. 5a, b). Like diorite gneiss, these mafic rocks also occur as inclusions within granodiorite and leucogranite. Their extent terminates within the granodiorite or leucogranite; hence the usage dyke-like or sill-like (Figs. 5a, b). Norite crosscuts diorite gneiss (Fig. 5b), with the mafic intrusion locally containing inclusions of the gneissic rock (Fig. 5c). Significantly, the anatectic leucosome-leucogranite exhibits liquid-liquid contact relation with the diorite gneiss and norite (Figs. 4g and 5c to e). Irregular lobate structures characterize the contact of leucogranite with diorite gneiss and norite (Fig. 5c). In contrast, the contact between diorite gneiss and norite is smooth and regular (Fig. 5c). Later pulses of leucogranite magmatism (veins) crosscut the norite (Fig. 5b). The co-mingling relation between the diorite gneiss, norite, and leucogranite is well preserved within the granodiorite (Figs. 5f to h).

4. Petrography and mineral chemistry

The diorite gneiss consists of plagioclase, quartz and biotite with accessory ilmenite, apatite, and zircon (Fig. 6a to c). Biotite typically occurs interstitial to felsic minerals and forms inclusions in them (Fig. 6a). Plagioclase is partially sericitized. A gneissic fabric is locally preserved. The dominant minerals have straight line and irregular grain margins (Fig. 6a, c). Both zircon and apatite exhibit euhedral-subhedral outlines (Fig. 6b, c). Zircons preserve oscillatory zoning typical of a magmatic origin (Fig. 6b). The onset of partial melting of the diorite gneiss is manifested by the appearance of K-feldspar and garnet (Fig. 6d to f). Myrmekite occur close to the plagioclase-K-feldspar interface (Figs. 6d, e). Irregular lobate grain margins with attenuated and cuspate shapes are conspicuous in this transition zone (Fig. 6d to f). Thin monazite rims occur on apatite (Fig. 6c). The leucocratic portion is characterized by an increase in the modal content of felsic minerals, including myrmekite (Fig. 6g). Plagioclase grains have a near-euhedral outline (Fig. 6g, h). Biotite is altered to chlorite (Fig. 6h).

The large composite sample selected for the U–Pb zircon geochronology was divided into two samples: GB3b and GB3. Both are garnet-bearing diorite gneiss, but GB3 is more leucocratic than GB3b. Large garnet porphyroblasts in sample GB3 contain abundant inclusions of biotite, quartz, plagioclase, and zircon (Fig. 7a to d). Grain boundaries are irregular lobate and protruding (Fig. 7a to d), as is typical of anatectic rocks. Zircons have subhedral or sub-rounded outlines and exhibit oscillatory zoning under BSE imaging (Fig. 7e, f). Monazite occurs along the zircon grain boundaries (Fig. 7e, f). GB3b (Qz-13/Pl-48/Grt-10/Bt-29; modal%) has essentially the same mineralogy as GB3 (Qz-15/Pl-52/Grt-12/Bt-21). It shows a lesser modal proportion of felsic minerals and smaller size of garnet grains than in GB3 (Fig. 7g, h). GB3b also contains subhedral or sub-rounded zircons with oscillatory zoning.

The norite sample (RN3) selected for U–Pb zircon geochronology is composed of plagioclase and orthopyroxene with accessory Fe–Ti oxides, apatite, and sulphides. Biotite occurs along the margin of orthopyroxene. The modal content of quartz, which is likely assimilated by the mafic intrusion, reaches 10 vol% (see Rajesh, 2019).

Microprobe analyses (the analytical conditions are given in DR1) of minerals in representative thin sections of the composite diorite gneiss samples are given in online Supplementary Material (Table DR2). Analyses of biotite and garnet in diorite gneiss from the Lose quarry obtained by Millonig et al. (2010) (sample Ma1h) are included for comparison in the different plots. Biotite shows $X_{Mg}^{Bt} = Mg/(Mg + Fe) = 0.49–0.51$, 0.13–0.16 apfu (atoms per formula unit) Ti, 1.53–1.57 apfu Al, and 0.68–0.82 wt% F + Cl (Fig. 8a; Table DR2a). Garnet has $X_{Mg}^{Grt} = Mg/(Mg + Fe^{2+}) = 0.13–0.18$, $X_{Ca} = Ca/(Ca + Mg + Fe^{2+}+Mn) = 0.04–0.05$ and $Mn = 0.14–0.18$ apfu (Fig. 8b; Table DR2b). Garnet grains are weakly zoned with X_{Mg}^{Grt} and X_{Ca}^{Grt} decreasing from core to both rims (Fig. 8c; Table DR2b). The anorthite [An (=Ca/Ca + Na + K)] content of plagioclase varies from An_{28} to An_{35} (Table DR2c). K-feldspar composition is Or_{85-96} (Table DR2c).

5. U–Pb zircon geochronology

5.1. Garnet-bearing diorite gneiss (GB3, 3b)

Zircons from GB3 and GB3b were analysed in situ in thin sections using laser ablation multi-collector inductively coupled plasma mass spectrometer (LA-MC-ICPMS) (see Supplementary online material DR1 for analytical details). Subhedral to sub-rounded zircon grains of 60 to 190 μm in diameter occur both in GB3 and GB3b (Fig. 9a to g). Prismatic outlines are locally preserved. BSE-SEM images of zircons are generally grey-homogenous, and show preserved oscillatory or sector

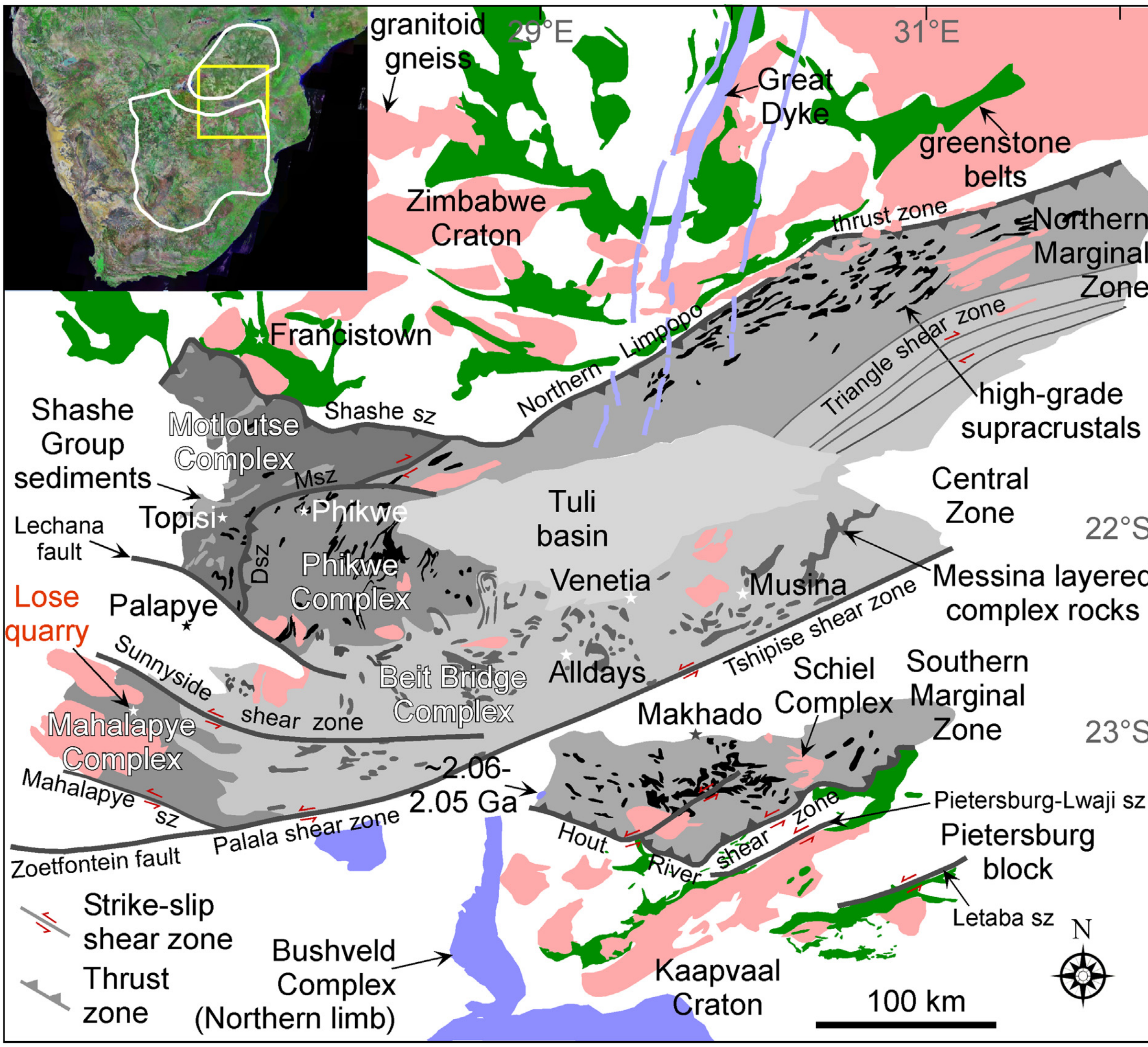

Fig. 3. Geological map of the Limpopo complex between the Archean Zimbabwe and Kaapvaal cratons (modified from Rajesh et al., 2020b). The central portion of this Paleoarchean to Paleoproterozoic terrane is referred to as the Central Zone, while those along the respective cratonic margins are the Northern Marginal Zone and the Southern Marginal Zone. The Central Zone includes the Beit Bridge Complex, Phikwe Complex and the Mahalapye Complex terranes. The Mahalapye Complex constitutes the westernmost terrane of the Limpopo Complex. The Motloutse Complex to the southwest of the Zimbabwe Craton is not part of the Limpopo Complex. sz – shear zone. Inset is the same as in Fig. 1. The box indicates the area covered in the main image.

zoning (Fig. 9a to g). Internal structures of zircon grains show domains with partially preserved zoning and unzoned domains where the zoning has been modified. This type of transgression of the unzoned domains is related to the recrystallization of magmatic zircons (e.g., Hoskin and Black, 2000; Pidgeon, 1992). The event that caused recrystallization had a magmatic component as evidenced by local preservation of oscillatory zoning in the outermost domain of zircon with near-prismatic outlines (e.g., Fig. 9g). The isotopic compositions of zircons from GB3 and GB3b are presented in Table 2 and are plotted in the concordia diagram (Fig. 9h). Representative BSE images indicating ablation spots and analytical numbers (Table 2) are given in Fig. 9a to g.

Thirty-eight LA-MC-ICPMS analyses were performed on zircons from samples GB3 and GB3b. Three analyses each from GB3 and GB3b were discarded due to high U contents up to 1300 ppm. These analytical spots correspond to patchy irregular outline (recrystallized?) lighter domains and gave apparent $^{207}Pb/^{206}Pb$ ages between 1193 Ma and 1977 Ma (e.g., see analytical spot 13 in Fig. 9c). The remaining analyses of zircons in both GB3 (2002 Ma – 2069 Ma; $n = 22$) and GB3b (2020 Ma – 2081 Ma; $n = 10$) gave uniform Paleoproterozoic apparent $^{207}Pb/^{206}Pb$ ages (Table 2). The respective U (87–383 ppm in GB3; 82–242 ppm in GB3b) and Th (7–134 ppm in GB3; 16–76 ppm in GB3b) contents, and Th/U ratios (GB3 = 0.14–0.63, one at 0.02; GB3b = 0.13–52; one at 0.09) are comparable (Table 2). Thirty-two analyses from GB3 and GB3b define a discordia with an upper intercept age of 2051 ± 6.8 Ma (Fig. 9h). In general, the oldest apparent $^{207}Pb/^{206}Pb$ age (≥ ~2.06 Ga) was obtained from unzoned or blurred zoned domains of zircon, while the respective apparent $^{207}Pb/^{206}Pb$ age from zoned domains are slightly younger (~2.05 Ga). Separate age recalculations for these two domains yielded a similar age of ~2.051 Ga. In view of the oscillatory zoning of the outermost domains of zircons, the upper intercept age is interpreted to represent the anatectic event in the diorite gneiss. The recrystallization of unzoned or blurred zoned zircon domains is likely related to this anatectic event.

5.2. Norite (RN3)

Zircons separated from sample RN3 were analysed using laser ablation quadrupole-based ICPMS (LA-Q-ICPMS). Analytical details are given in Supplementary online material DR1. Two types of zircons occur in sample RN3: elongate (100–250 μm diameter) and

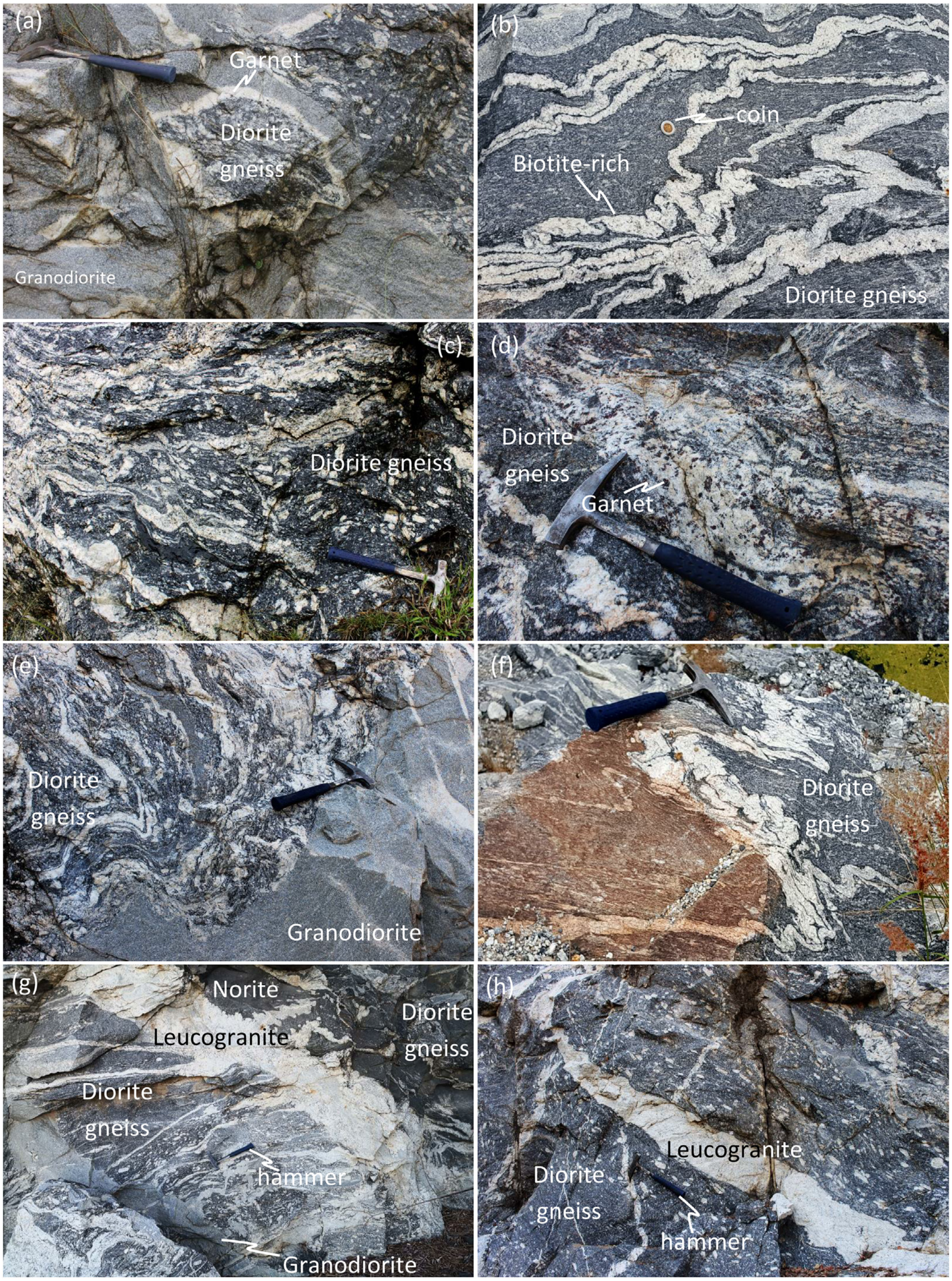

Fig. 4. Field photographs illustrating the partial melting of diorite gneiss and associated leucocratic portions, and their relation to adjacent rocks at the Lose quarry. (a) Inclusion of diorite gneiss with surrounding garnet-bearing leucosome within granodiorite. Both porphyritic and non-porphyritic varieties of diorite gneiss can be seen. Note the broken leucosome fragments with no biotite-rich margin and less irregular outline within granodiorite. (b) The diorite gneiss is migmatitic with local preservation of irregular outline leucosomes with biotite-rich margins. (c) Layer-parallel as well as cross-cutting leucosomes related to the partial melting of diorite gneiss. (d) Garnet formed during partial melting of the diorite gneiss and is locally seen in the gneissic rock, while it is widespread in the associated leucocratic portion. (e, f) Asymmetric structures related to melt segregation associated with partial melting of the diorite gneiss. In (e), the diorite gneiss and associated leucocratic portions occur as inclusion within the granodiorite. (g, h) The network of leucosomes to leucogranite veins to leucogranite dykes related to melt segregation associated with partial melting of diorite gneiss. Petrographic continuity exists between the leucosomes and leucogranite on different scales. Note the liquid-liquid contact relation between the leucogranite and norite in (g). Diorite gneiss occurs as inclusions within the norite. Granodiorite cross cuts all the rocks.

subhedral-anhedral (50–100 μm) (Fig. 10a to l). In general, the elongate (~3:1 to ~6:1) grains are characterized by prismatic outline and oscillatory zoning, with lighter luminescence under cathodeluminescence (CL) imaging (Fig. 10a to c). The elongate grains with partially preserved oscillatory zoning exhibit grey to lighter luminescence in CL images (Fig. 10e). A similar pattern of partial to well-preserved oscillatory zoning, respectively correlating with grey and lighter luminescence in CL images, is observed in the subhedral grains (Fig. 10d, f to h). No visible rims occur in both elongate and subhedral grains. Anhedral grains show rounded outline. In comparison to the elongate-subhedral grains,

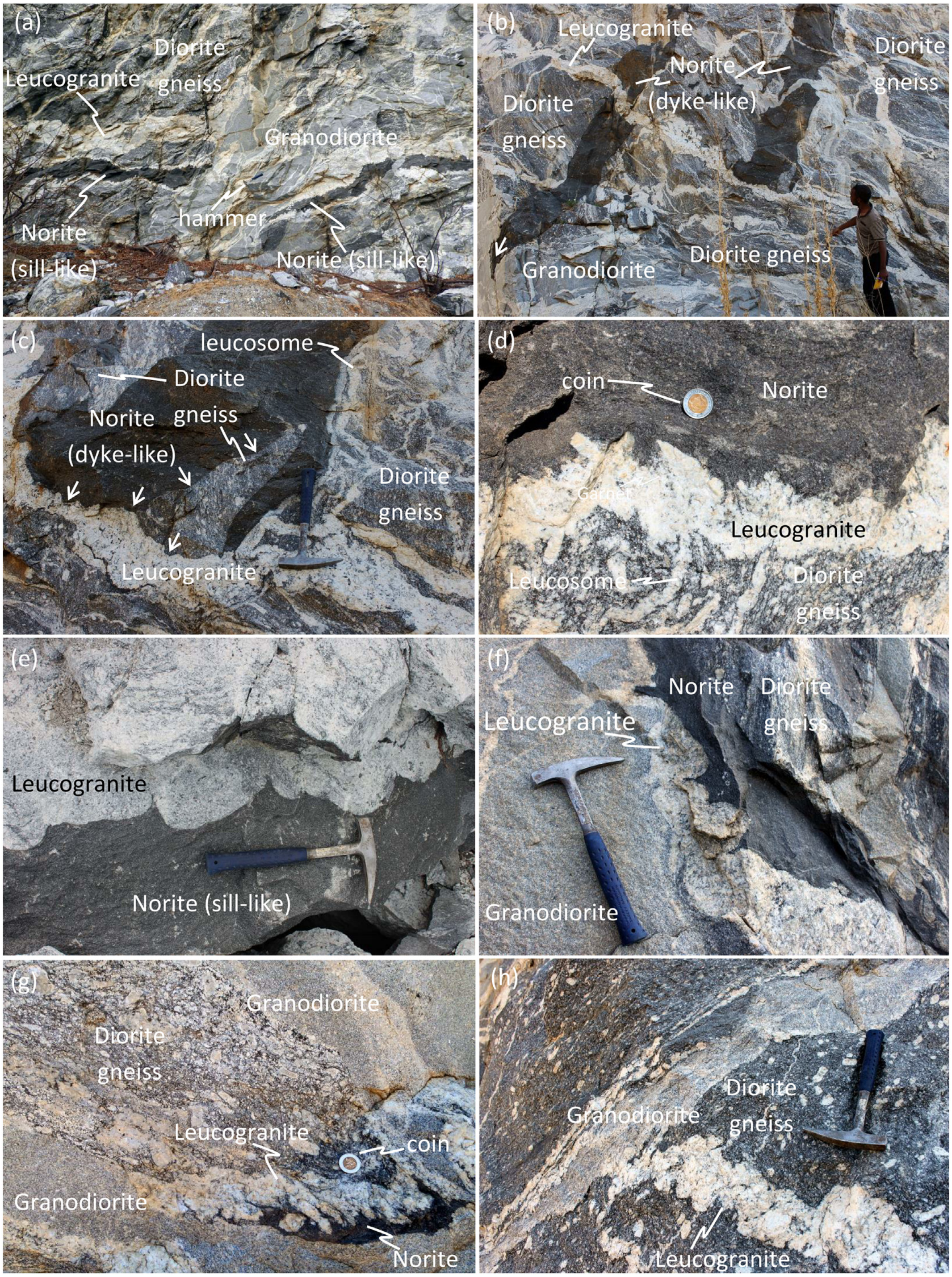

Fig. 5. Field photographs illustrating the relation between leucogranite, diorite gneiss, and norite at the Lose quarry. (a) Sill-like norite associated with leucogranite and diorite gneiss crosscut by granodiorite. Broken leucosome fragments with no biotite-rich margin and less irregular outline occur within the granodiorite. (b) The relationship between dyke-like norites, diorite gneiss, leucogranite, and granodiorite. Note the termination of the linear mafic body within the granodiorite – hence the usage dyke-like. (c) Differences in contact relations between the diorite gneiss, norite, and the leucogranite. The image is a close up of a portion of (b). Irregular lobate structures characterize the contact of leucogranite with diorite gneiss and norite. In contrast, the contact between the diorite gneiss and norite is smooth and regular. Note the diorite gneiss inclusion within the norite. (d) Petrographic continuity between leucogranite-leucosomes associated with diorite gneiss, and the liquid-liquid contact relation between leucogranite and norite. (e) Liquid-liquid contact relationships of leucogranite and a sill-like norite. (f) and (g) Three cotemporaneous rocks (diorite gneiss, norite, and leucogranite) occurring as a composite inclusion within the granodiorite. Note the liquid-liquid contact between the norite and leucogranite. (h) Diorite gneiss and associated leucogranite cross cut by granodiorite.

anhedral grains have complex internal structures (Fig. 10i to l). Multiple domains can be distinguished in terms of dark, grey and lighter luminescence in CL images (Figs. 10i to l). The isotopic compositions of zircons from sample RN3 are presented in Table 3 and are plotted in the concordia diagrams (Fig. 10m, n). Representative CL images of zircons with analytical spots and numbers (Table 3) are given in Fig. 10a to l.

Forty-four LA-Q-ICPMS analyses were performed on zircons from sample RN3. Thirty-nine analyses from the elongate-subhedral grains gave apparent $^{207}Pb/^{206}Pb$ ages between 1611 Ma and 2163 Ma, with

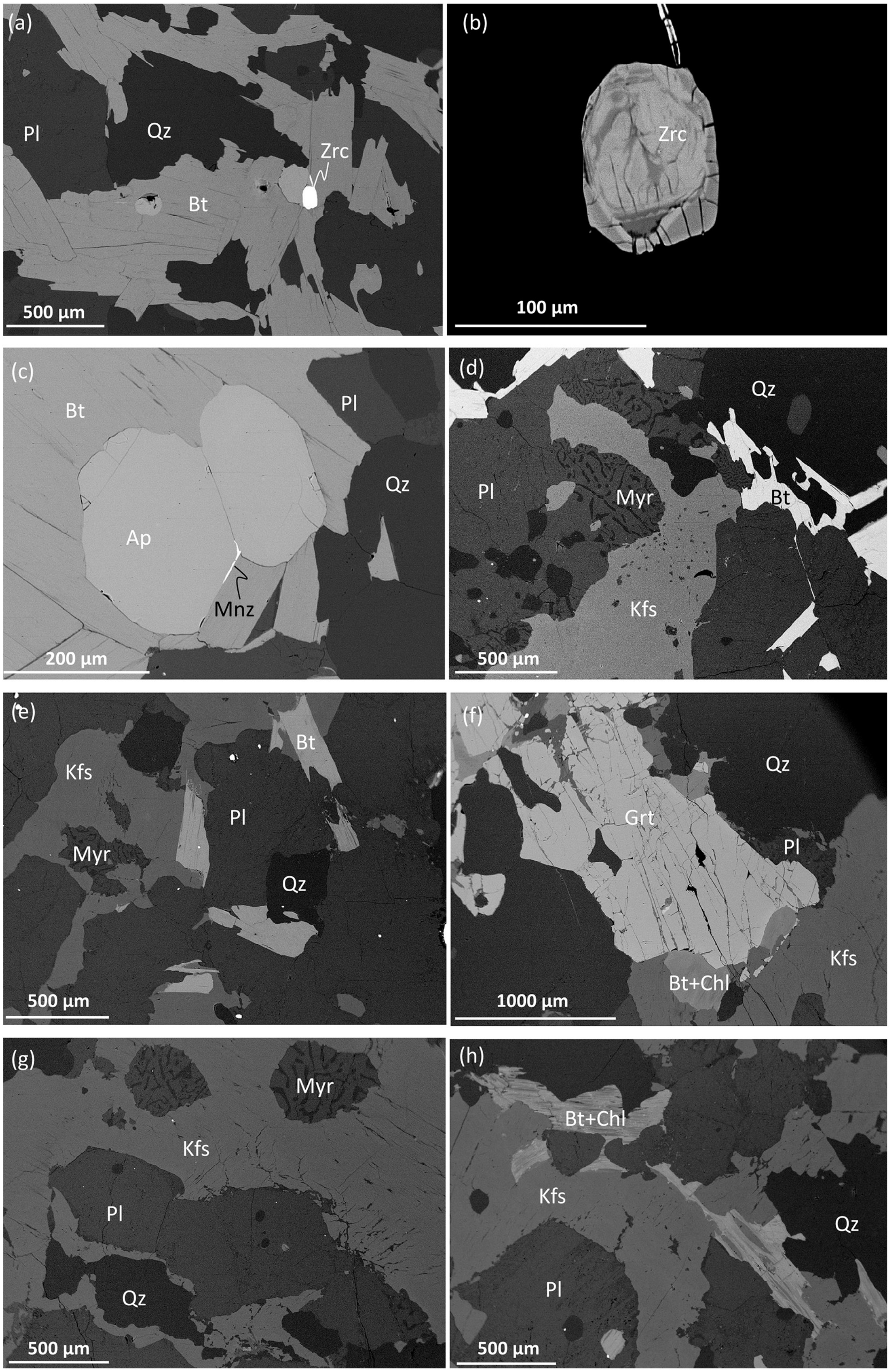

Fig. 6. Representative BSE images illustrating the change in mineralogy and texture related to the partial melting of biotite-bearing diorite gneiss from the Lose quarry. The images characterize the transition from diorite gneiss to an associated leucocratic portion. (a) Typical biotite-bearing diorite gneiss. Detailed image of the zircon (Zrc) is given in (b). (b) Zircon in diorite gneiss with euhedral-subhedral outlines preserves oscillatory zoning typical for zircons of magmatic origin. (c) Apatite with an euhedral-subhedral outline in the diorite gneiss. Note the thin rim of monazite on the apatite. (d), (e), (f) Onset of partial melting in the diorite gneiss is characterized by the appearance of K-feldspar (Kfs), myrmekite (Myr), and garnet (Grt). Myrmekite typically occurs close to the plagioclase-K-feldspar interface. (g) Plagioclase with near-euhedral outlines surrounded by K-feldspar, anhedral quartz (Qz), and myrmekite are characteristic of the leucocratic portion associated with diorite gneiss. (h) Biotite (Bt) is altered to chlorite (Chl) in the leucocratic portion.

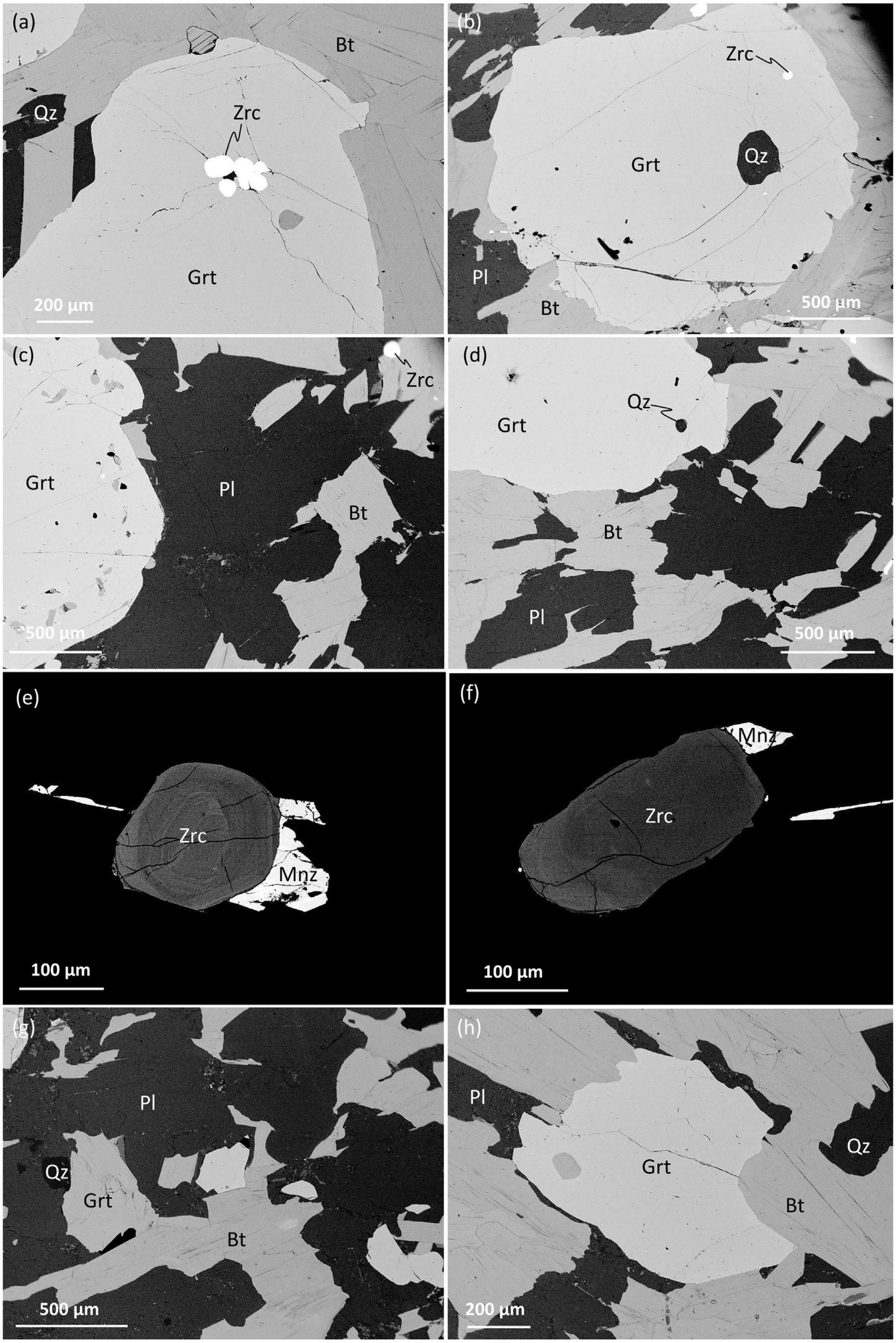

Fig. 7. Representative BSE images illustrating the mineralogy and texture of the two diorite gneiss samples GB3 and GB3B, sampled from a large composite sample, for U—Pb zircon geochronology. (a), (b), (c), (d) Large garnet porphyroblasts with widespread inclusions of biotite, quartz, plagioclase, and zircon characterize GB3. (e), (f) Zircons in both portions have a subhedral or sub-rounded outline and preserve oscillatory zoning under BSE imaging. Monazite (Mnz) grains occur along the margin of zircon. (g), (h) GB3B has a less modal proportion of felsic minerals with the garnet smaller in size than in GB3.

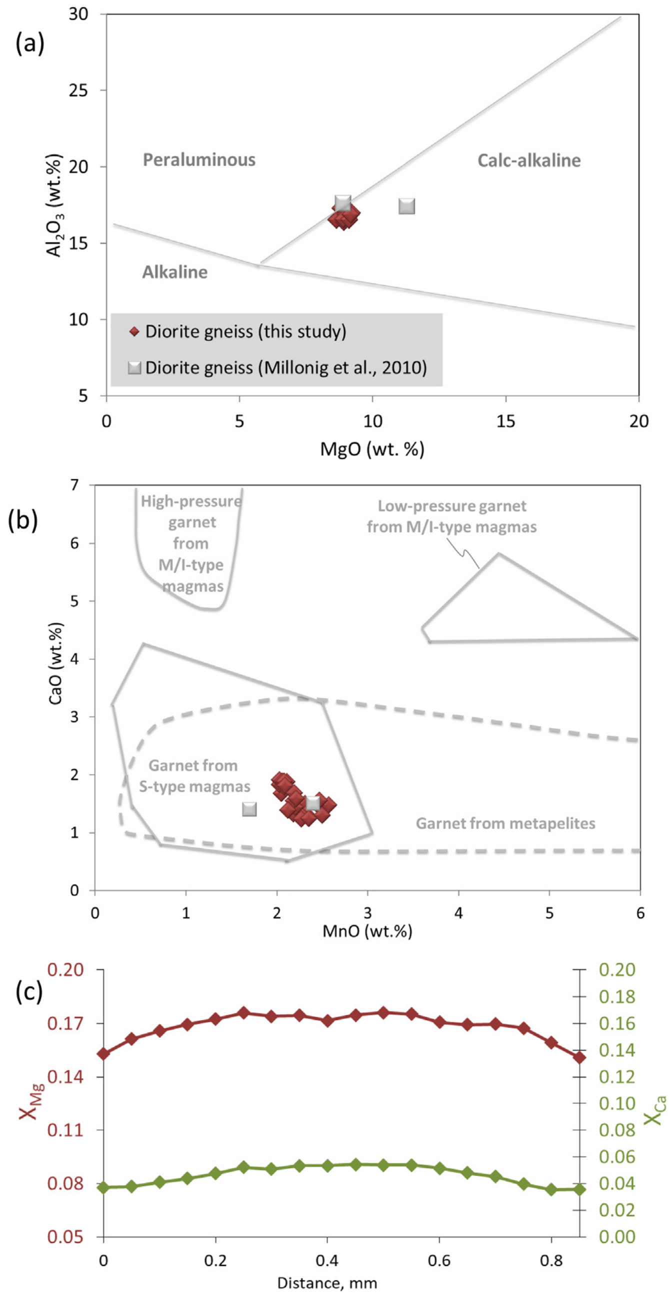

Fig. 8. Mineral chemistry-based diagrams illustrating the composition of biotite (a) and garnet (b) in garnet-bearing diorite gneiss from the Lose quarry. (c) Representative rim-core-rim profile in terms of X_{Mg} and X_{Ca} of garnet from the garnet-bearing diorite gneiss. Available chemical data on biotite and garnet in the garnet-bearing diorite gneiss from the Lose quarry studied by Millonig et al. (2010) (sample Ma1h) are included for comparison. Fields in (a) and (b) are respectively from Abdel-Rahman (1994) and Harangi et al. (2001).

a peak age distribution at ~2050 Ma (Fig. 10m). Nine least discordant analyses, with U contents of 132 to 479 ppm (one grain with 1152 ppm) and Th/U ratios of 0.09 to 0.42 (Table 3), define a concordia age of 2054 ± 7.9 Ma (Fig. 10n). Taking into account the oscillatory zoning of these zircons, the concordia age is interpreted to represent the crystallization of the norite. The remaining analyses are strongly discordant (>10% discordance) with widely varying U contents (13–1681 ppm; one grain with 10,816 ppm) and Th/U ratios (0.05–0.34; Table 3). These analyses approximately define a discordia with an upper intercept age of 2032 ± 46 Ma and a lower intercept age of 521 ± 150 Ma (not shown). The upper intercept age could indicate an overprint from a later granitic intrusion, while the lower intercept age is a common result of sub-recent weathering-related Pb loss in southern Africa (Kramers et al., 2009).

Five analyses from the core domains of anhedral grains gave older apparent $^{207}Pb/^{206}Pb$ ages of 2161 Ma, 2263 Ma, 2614 Ma, 2767 Ma and 2843 Ma (Fig. 10i to l, m; Table 3). Their U contents vary from 63 to 664 ppm with Th/U ratios of 0.02–0.25 (Table 3). Rounded outline and complex internal structures imply that these older zircons are likely xenocrysts.

6. Whole-rock geochemistry

Two samples of garnet-bearing diorite gneisses and two samples of associated leucogranite were selected for whole-rock geochemical analyses. Care was taken to isolate the representative portions from composite samples. Analytical conditions are given in Supplementary online material DR1. The bulk-rock compositions of the garnet-bearing diorite gneiss (samples GB3, GB3b) and leucogranite (LQ3, GB4) are given in Table 4. Available geochemical data on garnet-bearing diorite gneiss (sample Ma1h) from Millonig et al. (2010) and composition of melt predicted by phase equilibria modelling (GB3 melt composition; this study; see Section 7.2) are shown on the plots for comparison.

Garnet-bearing diorite gneiss samples show relatively low SiO_2 contents (~53–57 wt%). They are peraluminous, with A/CNK [= molar $Al_2O_3/(CaO + Na_2O + K_2O)$] values varying from 1.24 to 1.32 (Fig. 11a). They are ferroan [total Fe/ (total Fe + MgO) ≥ 0.8; Fig. 11b) and alkali-calcic to alkalic ($Na_2O + K_2O$-CaO > 2.8; Fig. 11c). The garnet-bearing diorite gneiss studied by Millonig et al. (2010) is comparable to less leucocratic GB3b (Fig. 11a to c). The leucogranite samples are slightly peraluminous (A/CNK = 1.03–1.04; Fig. 11a), magnesian to ferroan (Fig. 11b) and calc-alkalic to alkali-calcic (Fig. 11c). Along with a silica content of ~74–75 wt% and low $FeO_t + MgO + MnO + TiO_2$ content (0.31–0.87; Table 4), this is characteristic of peraluminous leucogranites (Frost et al., 2001).

Both the diorite gneiss and leucogranite have similar primitive-mantle normalized patterns with large ion lithophile element enrichment and relatively constant high-field strength elements (Fig. 11d). They show negative Ba, Th, Nb, Ta, P and Ti anomalies, and a positive U anomaly (Fig. 11d). In terms of the chondrite-normalized rare earth element (REE) pattern, both the diorite gneiss and the leucogranite are characterized by enrichment in light REE relative to middle REE [$(La/Sm)_N$ = 4.29–4.65 (diorite gneiss); 5.15–6.13 (leucogranite)]. They have variable heavy REE [HREE; $(Gd/Yb)_N$ = 0.52–0.57 (diorite gneiss); 0.79–1.64 (leucogranite)] and Eu anomalies [Eu/Eu* = 0.57–0.94 (diorite gneiss); 1.85–3.7 (leucogranite)] (see inset in Fig. 11d). In comparison to the leucogranite (ΣHREE = ~5–6), the higher HREE content of the diorite gneiss (ΣHREE = ~41–73; Table 4) is related to the higher modal content of garnet.

7. Discussion and concluding remarks

7.1. Nature of partial melting of diorite gneiss

The close association with the garnet-bearing diorite gneiss argues for an in situ origin of the leucosomes and leucogranite veins/dykes (see Fig. 4). Composite diorite gneiss samples containing the leucocratic portion represent a centimetre- to metre-scale transition from the onset of melting in the gneissic rock to the partial solidification of melt in the leucocratic portion (see Fig. 4). Irregular lobate grain margins, with attenuated and cuspate shapes, of the transition zone in the garnet-bearing diorite gneiss indicate its in situ origin (Fig. 6 and 7). Euhedral to subhedral plagioclase surrounded by K-feldspar and anhedral quartz, and myrmekites at the plagioclase-K-feldspar interface (see Fig. 6g), are indicative of partial solidification of melt in the leucocratic portion (e.g., Sawyer, 1999). Garnet and K-feldspar are typical peritectic phases produced during melting of a biotite-bearing protolith via the reaction

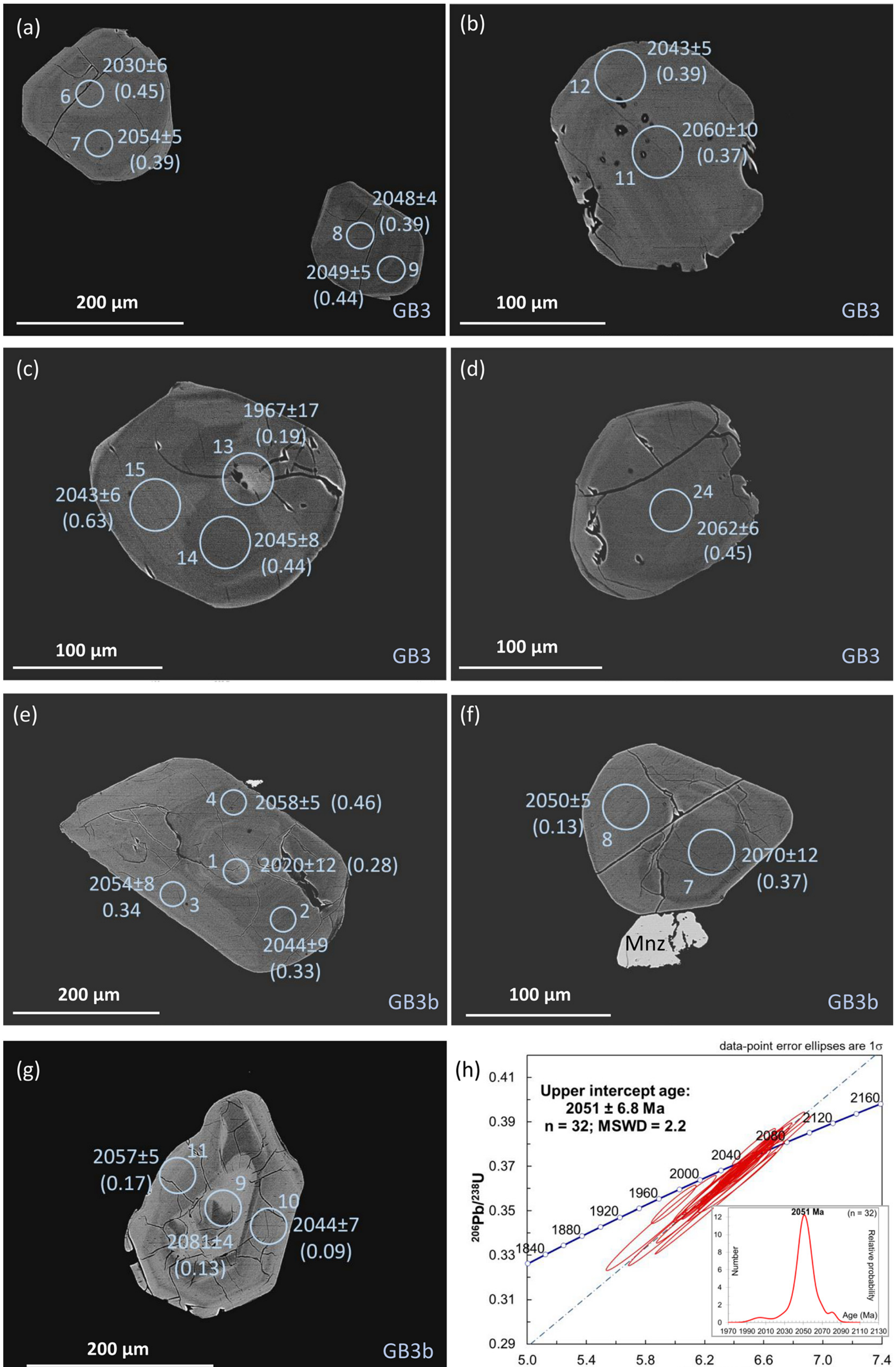

Fig. 9. Representative BSE images of zircons in GB3 (a to d) and GB3b (e to g) used for U—Pb zircon geochronology. Analytical spot, number, apparent $^{207}Pb/^{206}Pb$ age with 1σ error (in Ma) and Th/U ratio (in parenthesis) are indicated and correspond to the data given in Table 2. (h) Concordia diagram of U—Pb data for zircons from GB3 and GB3b.

Table 2
U—Pb data on zircons in GB3 and GB3b of a composite garnet-bearing diorite gneiss sample from the Lose quarry.

Sample-analysis no	U ppm	Th ppm	Th/U	$^{206}Pb/^{204}Pb$	Isotopic ratios													Age (Ga)						% Discordance
					$^{207}Pb/^{206}Pb$*	± 1 σ	$^{208}Pb/^{206}Pb$*	± 1 σ	$^{207}Pb/^{235}U$*	± 1 σ	$^{206}Pb/^{238}U$*	± 1 σ	Rho	$^{208}Pb/^{232}Th$*	± 1 σ	$^{232}Th/^{238}U$	± 1 σ	$^{206}Pb/^{238}U$	± 1 σ	$^{207}Pb/^{235}U$	± 1 σ	$^{207}Pb/^{206}Pb$	± 1 σ	
GB3-8-1	143	52	0.36	13,508	0.1264	0.0003	0.1154	0.0200	6.641	0.099	0.3811	0.0056	0.987	0.1202	0.0032	0.3659	0.0626	2081	26	2065	13	2048	4	1.9
GB3-8-2	152	70	0.46	10,390	0.1260	0.0004	0.1410	0.0247	6.578	0.102	0.3787	0.0058	0.983	0.1146	0.0029	0.4660	0.0804	2070	27	2056	14	2043	5	1.6
GB3-8-3	169	83	0.49	10,418	0.1264	0.0003	0.1329	0.0219	6.375	0.084	0.3658	0.0048	0.986	0.0975	0.0025	0.4983	0.0807	2009	22	2029	12	2049	4	−2.2
GB3-8-5	156	63	0.41	10,340	0.1231	0.0006	0.0978	0.0149	5.992	0.100	0.3529	0.0057	0.961	0.0845	0.0029	0.4086	0.0604	1948	27	1975	15	2002	8	−3.1
GB3-8-4	152	64	0.42	20,865	0.1270	0.0003	0.1156	0.0180	6.365	0.076	0.3635	0.0042	0.974	0.0993	0.0025	0.4232	0.0649	1999	20	2027	11	2057	5	−3.3
GB3-8-6	253	114	0.45	48,236	0.1251	0.0004	0.1215	0.0198	6.533	0.096	0.3788	0.0054	0.972	0.1016	0.0030	0.4529	0.0723	2070	25	2050	13	2030	6	2.3
GB3-8-7	145	56	0.39	21,386	0.1268	0.0004	0.1046	0.0163	6.316	0.069	0.3614	0.0038	0.966	0.0966	0.0024	0.3914	0.0600	1989	18	2021	10	2054	5	−3.7
GB3-8-8	186	72	0.39	14,042	0.1264	0.0003	0.1105	0.0184	6.578	0.069	0.3775	0.0039	0.975	0.1070	0.0026	0.3897	0.0640	2064	18	2056	9	2048	4	0.9
GB3-8-9	183	81	0.44	29,292	0.1264	0.0003	0.1193	0.0184	6.362	0.074	0.3649	0.0041	0.974	0.0972	0.0024	0.4482	0.0682	2006	19	2027	10	2049	5	−2.5
GB3-8-11	124	46	0.37	10,046	0.1272	0.0008	0.1081	0.0175	6.493	0.104	0.3703	0.0055	0.923	0.1078	0.0036	0.3712	0.0586	2031	26	2045	14	2060	10	−1.6
GB3-8-12	128	49	0.39	8403	0.1260	0.0003	0.1164	0.0193	6.419	0.082	0.3695	0.0046	0.978	0.1104	0.0029	0.3897	0.0637	2027	22	2035	11	2043	5	−0.9
GB3-8-14	168	74	0.44	37,509	0.1262	0.0006	0.1144	0.0174	6.268	0.133	0.3604	0.0074	0.974	0.0927	0.0043	0.4448	0.0639	1984	35	2014	19	2045	8	−3.5
GB3-8-15	214	134	0.63	13,529	0.1260	0.0004	0.1746	0.0269	6.250	0.133	0.3596	0.0076	0.987	0.0993	0.0044	0.6323	0.0921	1980	36	2011	19	2043	6	−3.6
GB3-8-16	209	41	0.20	19,151	0.1279	0.0003	0.0736	0.0148	6.504	0.276	0.3690	0.0156	0.998	0.1371	0.0079	0.1979	0.0371	2025	74	2046	37	2069	4	−2.5
GB3-8-17	87	32	0.37	4628	0.1269	0.0004	0.1036	0.0165	6.313	0.113	0.3609	0.0064	0.988	0.1013	0.0038	0.3689	0.0569	1986	30	2020	16	2055	5	−3.9
GB3-8-18	383	7	0.02	24,180	0.1269	0.0003	0.0121	0.0037	6.553	0.147	0.3745	0.0083	0.993	0.2349	0.0559	0.0194	0.0037	2050	39	2053	20	2056	4	−0.3
GB3-8-19	126	48	0.38	9978	0.1264	0.0004	0.1116	0.0183	6.436	0.091	0.3692	0.0051	0.975	0.1069	0.0033	0.3855	0.0619	2026	24	2037	12	2049	5	−1.3
GB3-8-20	136	57	0.42	105,874	0.1267	0.0004	0.1368	0.0278	6.389	0.224	0.3656	0.0128	0.996	0.1180	0.0049	0.4239	0.0830	2009	60	2031	31	2053	5	−2.5
GB3-8-21	205	30	0.14	23,801	0.1266	0.0003	0.0423	0.0072	6.448	0.080	0.3693	0.0045	0.985	0.1078	0.0033	0.1450	0.0242	2026	21	2039	11	2052	4	−1.5
GB3-8-22	153	97	0.63	10,991	0.1267	0.0004	0.1806	0.0322	6.363	0.122	0.3644	0.0069	0.989	0.1030	0.0033	0.6387	0.1114	2003	33	2027	17	2052	5	−2.8
GB3-8-23	180	87	0.48	11,225	0.1271	0.0004	0.1455	0.0240	6.044	0.113	0.3450	0.0063	0.984	0.1032	0.0041	0.4862	0.0772	1911	30	1982	16	2058	6	−8.3
GB3-8-24	168	76	0.45	11,212	0.1274	0.0005	0.1243	0.0202	6.427	0.098	0.3659	0.0054	0.968	0.1008	0.0032	0.4514	0.0717	2010	25	2036	13	2062	6	−3.0
GB3b-1	222	61	0.28	19,926	0.1244	0.0009	0.0947	0.0210	5.906	0.247	0.3445	0.0142	0.986	0.1176	0.0063	0.2775	0.0585	1908	68	1962	36	2020	12	−6.4
GB3b-2	82	27	0.33	8079	0.1261	0.0007	0.1053	0.0196	6.214	0.149	0.3576	0.0084	0.974	0.1140	0.0053	0.3303	0.0589	1971	40	2006	21	2044	9	−4.1
GB3b-3	103	35	0.34	10,447	0.1268	0.0006	0.1212	0.0243	6.027	0.228	0.3448	0.0129	0.992	0.1206	0.0062	0.3465	0.0658	1910	62	1980	33	2054	8	−8.1
GB3b-4	100	46	0.46	14,135	0.1271	0.0004	0.1459	0.0265	6.425	0.159	0.3666	0.0090	0.991	0.1146	0.0043	0.4667	0.0820	2014	43	2036	22	2058	5	−2.5
GB3b-7	127	46	0.37	12,759	0.1280	0.0009	0.1234	0.0236	6.447	0.193	0.3654	0.0106	0.972	0.1221	0.0053	0.3692	0.0679	2008	50	2039	26	2070	12	−3.5
GB3b-8	242	32	0.13	17,921	0.1265	0.0003	0.0416	0.0073	6.507	0.109	0.3731	0.0062	0.987	0.1155	0.0051	0.1343	0.0227	2044	29	2047	15	2050	5	−0.3
GB3b-9	216	28	0.13	19,534	0.1287	0.0003	0.0512	0.0102	6.273	0.270	0.3534	0.0152	0.998	0.1366	0.0068	0.1324	0.0250	1951	72	2015	38	2081	4	−7.2
GB3b-10	192	16	0.09	14,942	0.1261	0.0005	0.0323	0.0069	6.366	0.237	0.3662	0.0136	0.994	0.1379	0.0119	0.0859	0.0166	2012	64	2028	33	2044	7	−1.8
GB3b-11	111	19	0.17	7566	0.1270	0.0004	0.0593	0.0114	6.500	0.151	0.3713	0.0086	0.991	0.1270	0.0077	0.1733	0.0313	2035	40	2046	20	2057	5	−1.2
GB3b-13	143	76	0.53	12,495	0.1264	0.0004	0.1544	0.0262	6.710	0.111	0.3851	0.0062	0.980	0.1111	0.0044	0.5349	0.0880	2100	29	2074	15	2048	6	3.0

Rho is the error correlation defined as the quotient of the propagated errors of the $^{206}Pb/^{238}U$ and the $^{207}/^{235}U$ ratio.

* Common Pb corrected values; (1) Calculated using as ((1-(measured $^{206}Pb/^{238}U$ age/measured $^{207}Pb/^{206}Pb$ age))*100).

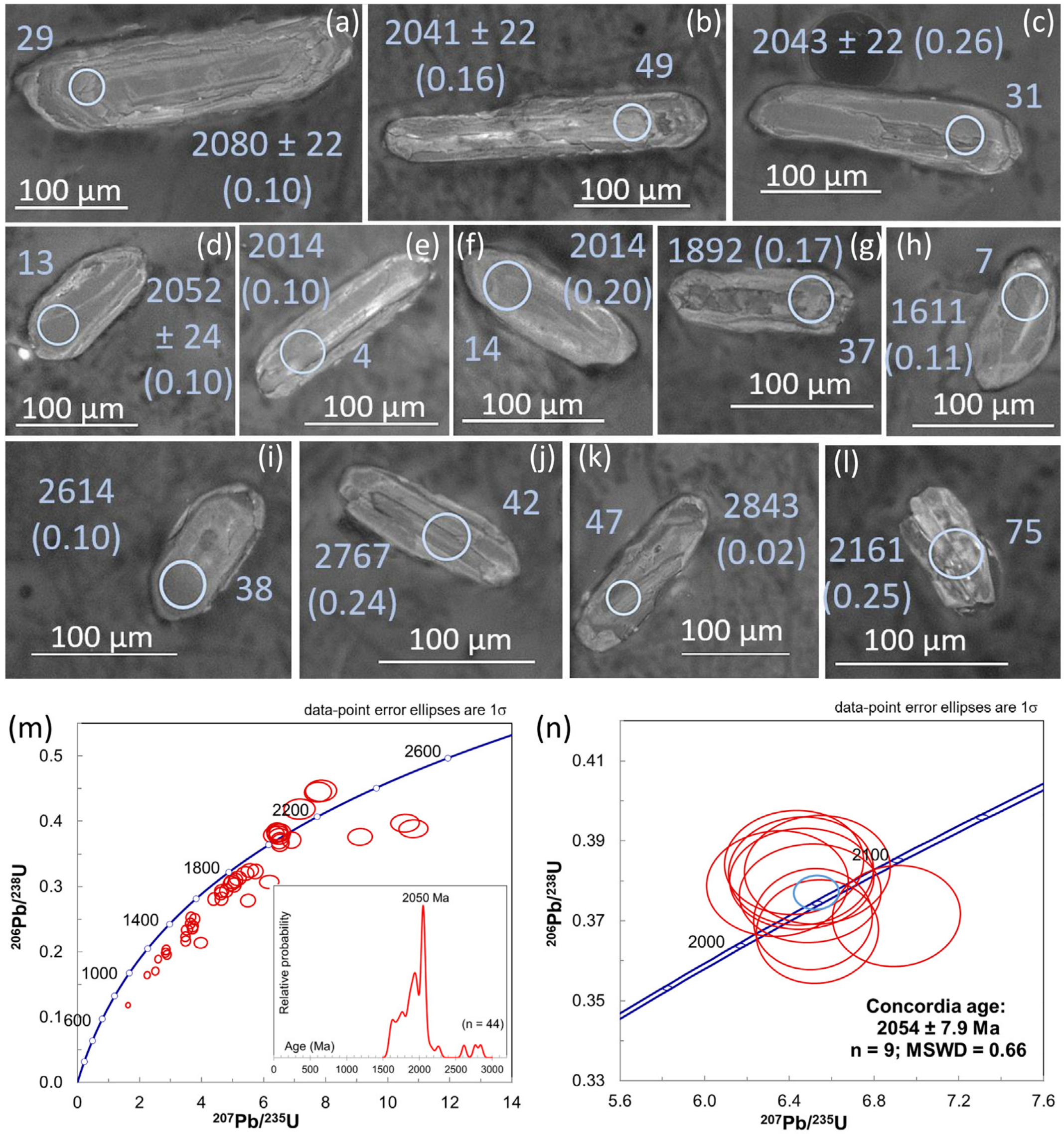

Fig. 10. Representative CL images of zircons in RN3 (a to l) used for U—Pb zircon geochronology. Analytical spot, number, Concordia age with 1σ error (in Ma) for least discordant analyses, apparent $^{207}Pb/^{206}Pb$ age (in Ma) for strongly discordant (>10% discordance) analyses and Th/U ratio (in parenthesis) are indicated. They correspond to the data given in Table 3. (m) Concordia diagram of all U—Pb data for zircons from RN3. Probability density distribution combining the Concordia ages for least discordant analyses and apparent $^{207}Pb/^{206}Pb$ ages for strongly discordant (>10% discordance) analyses are shown in the inset. (n) Concordia diagram of least discordant U—Pb data for zircons from RN3.

Bt + Pl + Qz ↔ Grt + Kfs + melt (e.g., Patiño Douce and Beard, 1996; Vielzeuf and Montel, 1994). In the rocks from the Lose quarry, this reaction is supported by the presence of garnet grains with inclusions of biotite, quartz and plagioclase (see Fig. 6 and 7). Monazite rims on apatite (Fig. 6c) from the transition zone resemble monazite rim grains on apatite margins resulting from the melting experiments of Wolf and London (1995). Similar textures involving monazite rim grains formed by the partial dissolution of apatite in the granitic melt has been described from other high-grade terranes (e.g., Harlov et al., 2007). Thus, along with newly formed K-feldspar and garnet, they represent the products of partial melting. Residual aqueous fluids that exsolved after crystallization of the melt likely caused alteration of the biotite to chlorite in the leucocratic portion (see Fig. 6h). Various textures reported here for partial melting of the diorite gneiss are comparable to those reported for the in situ melting of an amphibole-biotite tonalite gneiss at ~2.04 Ga, which formed thin orthopyroxene-bearing veins at the Causeway locality, central Limpopo Complex (Rajesh et al., 2013b, 2014a; Safonov et al., 2012).

7.2. Phase equilibria modelling of garnet-bearing diorite gneiss GB3

Phase equilibria modelling (details are given in supplementary online material DR1) for the garnet-bearing diorite gneiss GB3 (Table 4) was carried-out in the system MnO–Na_2O–CaO–K_2O–FeO–MgO–Al_2O_3–SiO_2–H_2O–TiO_2–O_2 (MnNCKFMASHTO).

Before modelling, the P-T conditions in the gneiss were estimated from the garnet-biotite-plagioclase-quartz equilibria using the winTWQ (version 2.32) software (Berman, 2007), with self-consistent end-member mineral properties according to Berman (1988) and the solid solution models of Berman and Aranovich (1996). Calculations showed a good convergence of end-member reactions within the temperature range 740–760 °C and the pressure range 6.6–7.2 kbar (Fig. 12).

Biotite is a principal Fe^{3+}-bearing phase in the diorite gneiss. Recalculation showed ~5.5–6 wt% Fe_2O_3 in the biotite (see Table DR2a). Taking into account 19–21 vol% of the biotite, the bulk Fe_2O_3 content of the gneiss GB3 was estimated to be about 1 wt%. Therefore, the pseudosections for the GB3 gneiss were calculated with a “free” O_2 (as

Table 3
U—Pb data on zircons in the norite sample RN3 from the Lose quarry.

Sample	Grain #	U ppm	Th/U		Isotopic ratios						Age (Ga)						Concordia age [1]	± 1 σ	% Discordance [2]
				$^{204}Pb/^{206}Pb$	$^{206}Pb^*/^{238}U$	± 1 σ	$^{207}Pb^*/^{235}U$	± 1 σ	$^{207}Pb^*/^{206}Pb^*$	± 1 σ	$^{206}Pb/^{238}U$	± 1 σ	$^{207}Pb/^{235}U$	± 1 σ	$^{207}Pb/^{206}Pb$	± 1 σ	(Ma)		
RN3	50	221	0.42	0	0.379	0.009	6.343	0.221	0.121	0.003	2.073	0.041	2.024	0.030	1.975	0.046	2041	25	5.0
RN3	49	405	0.16	0.0004	0.367	0.009	6.532	0.191	0.129	0.002	2.017	0.040	2.050	0.025	2.085	0.029	2041	22	3.3
RN3	31	479	0.26	0.0000	0.370	0.008	6.512	0.185	0.128	0.002	2.031	0.039	2.048	0.025	2.063	0.032	2043	22	1.5
RN3	13	224	0.10	0.0001	0.377	0.008	6.498	0.221	0.125	0.003	2.062	0.038	2.046	0.029	2.029	0.046	2052	24	1.6
RN3	20	132	0.47	0	0.381	0.008	6.459	0.225	0.123	0.003	2.079	0.039	2.040	0.030	2.002	0.046	2055	24	3.8
RN3	65	235	0.09	0	0.382	0.009	6.455	0.226	0.122	0.003	2.088	0.041	2.040	0.030	1.992	0.044	2056	25	4.8
RN3	41	1152	0.16	0	0.385	0.009	6.422	0.217	0.121	0.003	2.098	0.040	2.035	0.029	1.973	0.044	2057	24	6.3
RN3	70	390	0.14	0	0.383	0.009	6.531	0.228	0.124	0.003	2.089	0.042	2.050	0.030	2.012	0.044	2063	25	3.8
RN3	29	226	0.10	0.0011	0.371	0.008	6.905	0.199	0.135	0.002	2.035	0.039	2.099	0.025	2.163	0.032	2080	22	5.9
RN3	26	1054	0.34	0.0003	0.234	0.005	3.530	0.119	0.109	0.003	1.355	0.027	1.534	0.026	1.792	0.044	–	–	24.4
RN3	45	1226	0.10	0.0001	0.307	0.007	4.992	0.169	0.118	0.003	1.727	0.034	1.818	0.028	1.924	0.044	–	–	10.2
RN3	36	1681	0.08	0.0001	0.294	0.006	4.649	0.156	0.115	0.003	1.659	0.032	1.758	0.028	1.877	0.046	–	–	11.6
RN3	60	992	0.12	0	0.313	0.007	5.169	0.178	0.120	0.003	1.754	0.035	1.847	0.029	1.953	0.046	–	–	10.2
RN3	24	500	0.32	0	0.320	0.007	5.407	0.182	0.123	0.003	1.788	0.034	1.886	0.028	1.995	0.046	–	–	10.3
RN3	4	751	0.10	0.0005	0.325	0.007	5.549	0.184	0.124	0.003	1.813	0.033	1.908	0.028	2.014	0.044	–	–	10.0
RN3	59	1153	0.12	0.0001	0.305	0.007	4.954	0.170	0.118	0.003	1.715	0.035	1.811	0.029	1.924	0.046	–	–	10.9
RN3	3	982	0.05	0.0001	0.189	0.004	2.597	0.072	0.100	0.002	1.116	0.022	1.300	0.020	1.616	0.034	–	–	31.0
RN3	6	726	0.23	0.0005	0.253	0.005	3.651	0.102	0.105	0.002	1.455	0.028	1.561	0.022	1.707	0.032	–	–	14.8
RN3	7	808	0.11	0.0005	0.164	0.004	2.252	0.063	0.099	0.002	0.981	0.020	1.198	0.020	1.611	0.034	–	–	39.1
RN3	8	236	0.08	0.0004	0.236	0.005	3.710	0.108	0.114	0.002	1.363	0.027	1.573	0.023	1.868	0.034	–	–	27.0
RN3	10	385	0.25	0	0.224	0.005	3.484	0.100	0.113	0.002	1.301	0.026	1.524	0.022	1.848	0.032	–	–	29.6
RN3	11	108160	0.09	0.0005	0.118	0.003	1.633	0.046	0.100	0.002	0.720	0.015	0.983	0.018	1.626	0.034	–	–	55.7
RN3	21	562	0.26	0.0002	0.244	0.005	3.645	0.104	0.108	0.002	1.406	0.028	1.559	0.022	1.775	0.032	–	–	20.8
RN3	25	587	0.11	0.0001	0.250	0.006	3.780	0.108	0.110	0.002	1.440	0.029	1.588	0.023	1.792	0.032	–	–	19.7
RN3	37	409	0.17	0	0.289	0.007	4.621	0.134	0.116	0.002	1.639	0.033	1.753	0.024	1.892	0.032	–	–	13.4
RN3	40	253	0.17	0.0009	0.294	0.007	4.800	0.142	0.119	0.002	1.660	0.033	1.785	0.024	1.934	0.034	–	–	14.2
RN3	43	748	0.12	0.0006	0.323	0.007	5.734	0.164	0.129	0.002	1.803	0.036	1.937	0.024	2.083	0.029	–	–	13.4
RN3	46	552	0.27	0.0000	0.281	0.006	4.396	0.128	0.113	0.002	1.596	0.033	1.712	0.024	1.855	0.032	–	–	14.0
RN3	51	596	0.06	0.0002	0.199	0.005	2.837	0.084	0.104	0.002	1.167	0.025	1.365	0.022	1.689	0.034	–	–	30.9
RN3	52	265	0.06	0.0007	0.281	0.007	4.639	0.139	0.120	0.002	1.598	0.033	1.756	0.025	1.951	0.032	–	–	18.1
RN3	58	152	0.10	0.0002	0.303	0.007	5.045	0.155	0.121	0.002	1.704	0.035	1.827	0.026	1.970	0.034	–	–	13.5
RN3	64	332	0.23	0.0008	0.196	0.005	2.886	0.088	0.107	0.002	1.152	0.025	1.378	0.023	1.748	0.034	–	–	34.1
RN3	66	1005	0.29	0.0005	0.170	0.004	2.508	0.074	0.107	0.002	1.014	0.022	1.274	0.021	1.743	0.034	–	–	41.8
RN3	69	1532	0.29	0.0002	0.203	0.005	2.859	0.084	0.102	0.002	1.192	0.026	1.371	0.022	1.660	0.034	–	–	28.2
RN3	76	635	0.12	0.0001	0.309	0.007	5.094	0.151	0.119	0.002	1.738	0.037	1.835	0.025	1.948	0.029	–	–	10.8
RN3	77	433	0.07	0.0005	0.217	0.005	3.490	0.106	0.117	0.002	1.264	0.028	1.525	0.024	1.909	0.032	–	–	33.8
RN3	30	17	0.17	0.0003	0.447	0.011	7.852	0.334	0.127	0.004	2.381	0.048	2.214	0.038	2.063	0.061	–	–	15.4
RN3	34	55	0.17	0	0.445	0.010	7.753	0.283	0.126	0.004	2.373	0.045	2.203	0.032	2.048	0.049	–	–	15.9
RN3	14	13	0.20	0	0.419	0.010	7.156	0.331	0.124	0.005	2.254	0.047	2.131	0.040	2.014	0.068	–	–	11.9
RN3	75	63	0.25	0.0029	0.214	0.005	3.974	0.139	0.135	0.003	1.250	0.028	1.629	0.028	2.161	0.042	–	–	42.1
RN3	39	299	0.20	0.0017	0.279	0.006	5.495	0.160	0.143	0.003	1.585	0.032	1.900	0.025	2.263	0.032	–	–	30.0
RN3	38	520	0.10	0.0048	0.376	0.009	9.115	0.260	0.176	0.003	2.058	0.040	2.350	0.026	2.614	0.028	–	–	21.3
RN3	42	664	0.24	0.0055	0.397	0.009	10.562	0.301	0.193	0.003	2.156	0.042	2.485	0.026	2.767	0.028	–	–	22.1
RN3	47	503	0.02	0.0062	0.389	0.009	10.831	0.311	0.202	0.003	2.117	0.042	2.509	0.026	2.843	0.028	–	–	25.5

(1) Calculated $^{207}Pb/^{206}Pb$ age using measured $^{206}Pb/^{238}U$ ratio ± 1 sigma error; $^{207}Pb/^{235}U$ ratio ± 1 sigma error and the error correlation value (Rho)
(2) Calculated using as ablsolute value ((1-(measured $^{206}Pb/^{238}U$ age/measured $^{207}Pb/^{206}Pb$ age))*100)
Rho is the error correlation defined as the quotient of the propagated errors of the $^{206}Pb/^{238}U$ and the $^{207}/^{235}U$ ratio.
* Common Pb corrected values.

Table 4
Major, trace, and rare earth element data of garnet-bearing diorite gneiss and associated leucogranite from the Lose quarry.

Sample No.	GB3	GB3b	GB4	LQ3
Rock type	Diorite gn	Diorite gn	Leucogranite	Leucogranite
SiO_2 (wt%)	57.35	53.39	75.48	74.2
TiO_2	0.59	0.89	0.02	0.05
Al_2O_3	18.9	19.56	13.67	14.15
Fe_2O_3*	9.96	12.78	0.24	0.68
MnO	0.24	0.38	0.005	0.005
MgO	2.46	2.77	0.04	0.13
CaO	3.41	3.33	1.18	1.37
Na_2O	3.92	3.6	2.82	3.04
K_2O	2.39	2.61	6.03	5.69
P_2O_5	0.03	0.02	0.04	0.03
Cr_2O_3	0.032	0.039	0.012	0.036
LOI	0.50	0.40	0.30	0.50
Total	99.81	99.81	99.95	99.96
$Na_2O + K_2O$-CaO	2.90	2.88	7.67	7.36
total Fe/(total Fe + MgO)	0.80	0.82	0.86	0.84
FeMnMgTi	13.25	16.82	0.31	0.87
ASI	1.24	1.32	1.03	1.04
Mg#	33.60	30.75	25.46	28.15
Na_2O/K_2O	1.64	1.38	0.47	0.53
CaO/Na_2O	0.87	0.93	0.42	0.45
Ba (ppm)	220	245	1091	960
Ni	41	52	<20	<20
Sc	30	45	<1	<1
Be	1	2	<1	1
Co	20.6	24.6	0.5	1.2
Cs	3.7	3.1	1.3	0.7
Ga	23.2	18.4	11.3	12.2
Hf	8.6	5.2	2	0.7
Nb	10.6	11.7	0.6	2.2
Rb	147.6	166.2	147.1	142.7
Sn	<1	<1	<1	<1
Sr	172.6	167.7	145.8	203.1
Ta	1	0.9	0.2	0.2
Th	4.3	5.1	4	7
U	3.7	2	21.9	6.3
V	111	121	8	26
W	1.9	<0,5	<0,5	1.1
Zr	302.7	188.4	55.2	21.1
Y	78	142.1	8.8	9.4
La	17.5	26.7	7.5	13
Ce	28.3	43.8	11.9	23.3
Pr	2.96	4.49	1.09	2.48
Nd	10	16.3	3.9	8.4
Sm	2.43	4.02	0.79	1.63
Eu	1.12	1.21	1.06	0.97
Gd	5.21	9.52	0.97	1.53
Tb	1.34	2.46	0.19	0.23
Dy	11.4	21.69	1.38	1.58
Ho	2.93	5.31	0.31	0.29
Er	9.38	16.25	0.94	0.89
Tm	1.34	2.3	0.15	0.12
Yb	8.24	13.91	1.02	0.77
Lu	1.2	2.03	0.15	0.11
$(La/Sm)_N$	4.65	4.29	6.13	5.15
$(Gd/Yb)_N$	0.52	0.57	0.79	1.64
$(La/Yb)_N$	1.52	1.38	5.27	12.11
Eu/Eu*	0.94	0.57	3.70	1.85
ΣHREE	41.04	73.47	5.11	5.52

Total Fe as Fe_2O_3; LOI - loss on ignition; FeMnMgTi = total Fe + MnO + MgO + TiO_2.
ASI = molar Al_2O_3/((CaO-1,67*P_2O_5) + Na_2O + K_2O); Mg# = 100.Mg/(Mg + Fe^{2+}); FeO = Fe_2O_3/1.15.
Eu/Eu* = Eu_N/((Sm_N+ Gd_N)/2); N - chondrite normalized (Sun and McDonough, 1989).

a monitor of Fe_2O_3) content 0.1 wt%. An optimal water content was specified using the T-M_{H2O} (where M_{H2O} is water content in the system) at 7.0 kbar (Fig. 13a), which corresponds to the average pressure value estimated using the TWQ method (Fig. 12). Calculations showed that the best convergence of mineral isopleths N^{Grt}_{Mg} = 100 Mg/(Mg + Fe_t + Ca + Mn) = 0.16–0.17, N^{Grt}_{Ca} = 100Ca/(Mg + Fe_t + Ca + Mn) = 0.04–0.05, X^{Bt}_{Mg} = 100 Mg/(Mg + Fe_t) = 0.42–0.43, and X^{Pl}_{Ca} = 100Ca/(Ca + Na + K) = 0.29–0.30 for sample GB3 (where Fe_t is total Fe) was at M_{H2O} about 0.7 wt% (Fig. 13a). For this water content, the H_2O does not appear as a free fluid phase in the subsolidus, and K-feldspar is absent in the assemblage (Fig. 13a).

Most portions of the P-T pseudosection, constructed for the composition GB3 (Table 4) at M_{H2O} = 0.7 wt% (Fig. 13b), is occupied by the melt + Grt + Bt + Pl + Ilm + Qz field, a mineral assemblage which is characteristic for this sample. Superposition of the above isopleths N^{Grt}_{Mg} and N^{Bt}_{Mg} correspond to temperatures of about 730 °C, while isopleths N^{Grt}_{Ca} and N^{Pl}_{Ca} demarcate pressures of 7.2–7.5 kbar (Fig. 13b). These values are in good agreement with the estimates using the winTWQ software (Fig. 12). In addition, the biotite TiO_2 content (2.0–2.1 wt%), predicted for this P-T condition, is close to that in the actual biotites from the sample. This P-T region corresponds to the field melt + Grt + Bt + Pl + Ilm + Qz just above the solidus (Fig. 13b). The estimated modal proportion of the minerals (vol%), Grt ~8, Bt ~19, Pl ~56, Qz ~17, and Ilm ~0.4, is very close to those observed for sample GB3. The melt content in the system between 720 and 750 °C is just 0.3–1 vol%. The melt composition (calculated for 730 °C and 7.3 kbar) is as follows (wt%): SiO_2–67.21, Al_2O_3–13.74, FeO – 0.30, MgO – 0.07, CaO – 0.47, Na_2O – 4.07, K_2O – 4.30, and H_2O – 9.84. The melt composition, re-calculated on a H_2O-free basis (GB3 melt composition), shows a good correspondence with the chemistry of the leucogranites (GB4, LQ3) associated with the garnet-bearing diorite gneiss (see Fig. 11a to c). The position of the isopleths in Fig. 13b shows that weak zoning in the garnet with a decrease of Mg and Ca within 2–3 mol% from the cores to the rims reflects a slight decrease in the P-T parameters below the solidus. Along this path, the biotite Mg-number remains almost constant. The estimated P-T conditions are comparable to those reported by Millonig et al. (2010) for the Mahalapye diorite gneiss.

7.3. Timing of the anatectic event

The timing of the anatectic event that resulted in the formation of the leucogranite can be addressed in terms of the mutual relationships between the diorite gneiss, leucogranite, norite, and granodiorite. Both the 2061 ± 6 Ma (Zeh et al., 2007) diorite gneiss and associated leucogranite are cross cut by the 2039 ± 9 Ma (Millonig et al., 2010) granodiorite (see Fig. 5a). The occurrence of leucosomes as fragments within the granodiorite (Fig. 4a and 5a) indicate that they were likely assimilated upon segregation from the diorite gneiss. The norites were emplaced as sharp-edged dykes and sills into the diorite. Importantly, they have liquid-liquid interfaces against leucosomes and leucogranite (see Fig. 5). The norite shows a *syn*-Bushveld age, 2054 ± 7.9 Ma (see Fig. 10n). These field relationships indicate co-mingling between diorite gneiss, norite, and leucogranite (see Figs. 4g and 5c to e). The three contemporaneous rocks occur as composite inclusions within the granodiorite (see Fig. 5f, g). Thus, the age of the anatectic event that led to the formation of the leucogranite should be between ~2.06 Ga (diorite gneiss) and ~2.04 Ga (granodiorite) (Fig. 5h), and, more precisely, closer to that of the norite (~2.05 Ga).

The zircons grains in the 2061 ± 6 Ma diorite gneiss (Zeh et al., 2007) exhibit typical magmatic oscillatory zoning. Similar oscillatory zoned zircons with near prismatic outlines occur in normal (garnet-absent) diorite gneiss (see Fig. 6b). Millonig et al. (2010) presented a concordant U–Pb monazite age of 2045 ± 8 Ma from the garnet-bearing diorite gneiss. Monazite grains typically occur along the zircon grain boundaries (see Figs. 7e, f and 9f). Thus, the ~2.045 Ga age should be slightly younger than the anatectic event. Millonig et al. (2010) pointed out that granodiorite cross cuts the dated garnet-bearing diorite gneiss. Hence, the ~2.045 Ga age seems to be an earlier pulse of the granodiorite magma. These authors also presented a Lu–Hf isochron age of 2039·6 ± 1·3 Ma from three garnet fractions combined with zircon Lu–Hf isotope data previously obtained by Zeh et al. (2007). As zircon occurs as inclusions in garnet (see Fig. 7a), while garnet and monazite

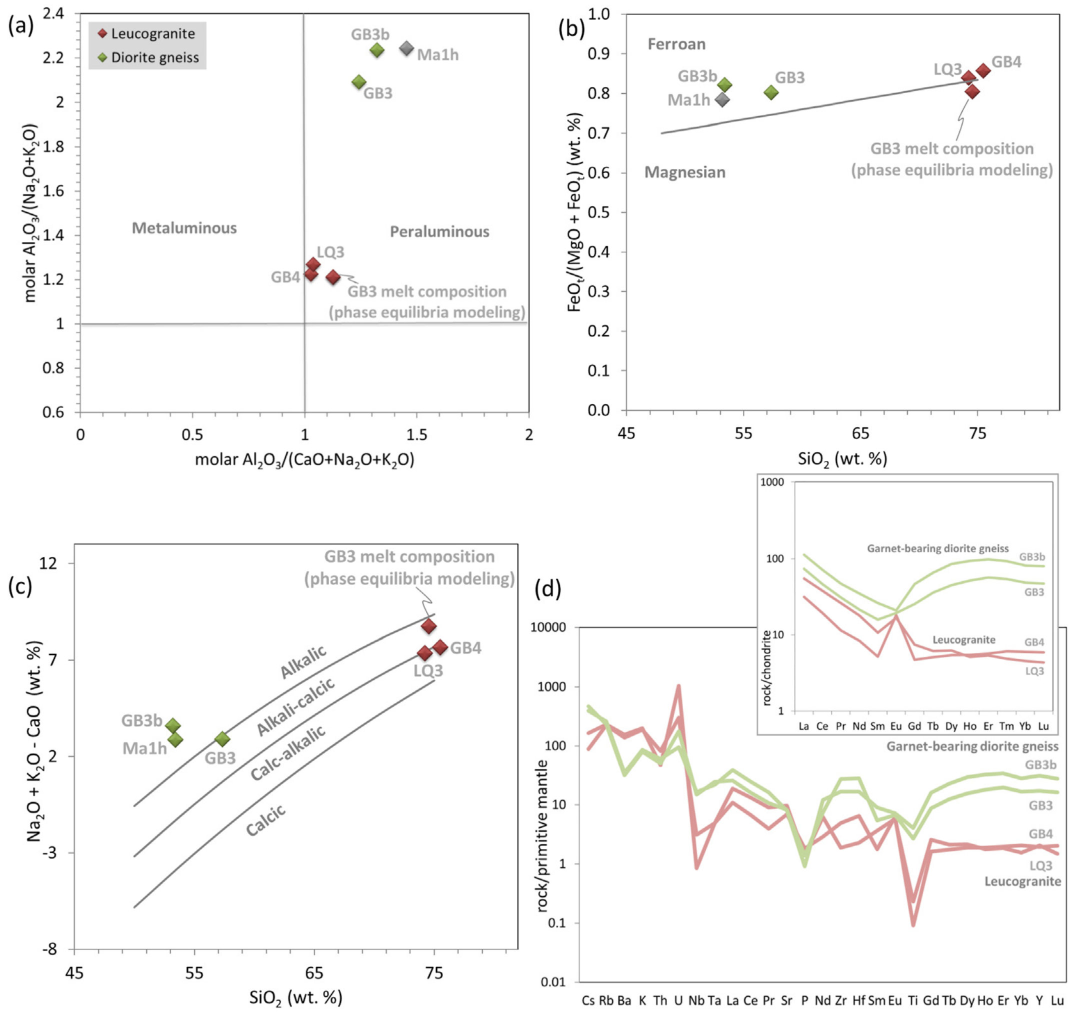

Fig. 11. Whole-rock geochemistry diagrams illustrating the composition of the garnet-bearing diorite gneiss (GB3, GB3b) and associated leucogranite (LQ3, GB4) from the Lose quarry. (a) molar $Al_2O_3/(CaO + Na_2O + K_2O)$ versus molar $Al_2O_3/(Na_2O + K_2O)$ plot. (b) $FeO_t/(FeO_t + MgO)$ versus SiO_2 plot. (c) $Na_2O + K_2O$-CaO versus SiO_2 plot. (d) Primitive mantle-normalized (Sun and McDonough, 1989) trace element spidergram and chondrite-normalized (Sun and McDonough, 1989) REE diagram (inset). Available geochemical data on the garnet-bearing diorite gneiss (Ma1h) from Millonig et al. (2010) and the composition of melt predicted by phase equilibria modelling (GB3 melt composition; this study) are included in (a) to (c). The fields in (b) and (c) are from Frost et al. (2001).

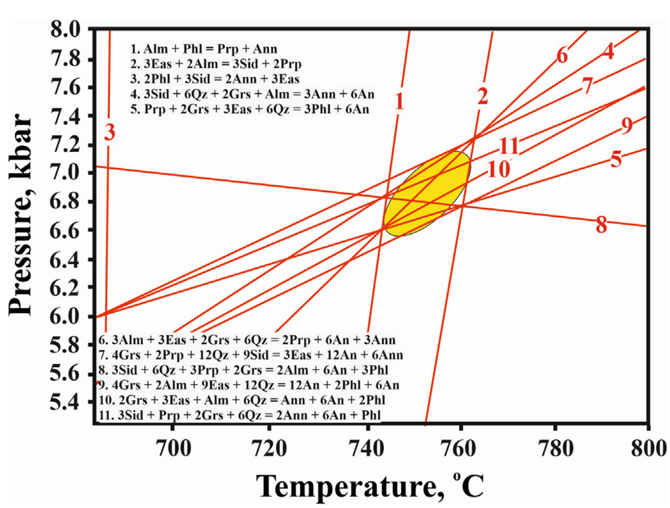

Fig. 12. P-T estimate for the diorite gneiss GB3 using the winTWQ software. Red lines marked by numbers are individual end-member reactions. Yellow ellipse shows the region of convergence for the reactions. (For interpretation of the references to colour in this figure legend, the reader is referred to the web version of this article.)

formed during the metamorphic overprint, the Lu–Hf isochron age cannot reflect the crystallization age of garnet (see Millonig et al., 2010).

Zircons from the garnet-bearing diorite gneiss containing leucocratic portions that were dated in the present study are slightly different from those described in previous studies. The magmatic origin of the protolith of the diorite gneiss is evident from oscillatory zoning and local preservation of near-prismatic outlines of the zircons (see Fig. 9a to g). But these magmatic zircon domains are recrystallized. Oscillatory zoned outermost portions (see Fig. 9g) support the inference that the recrystallization was likely caused by the anatectic event. Thus, we deduce an age of 2051.3 ± 6.8 Ma for the anatexis of the diorite gneiss that resulted in the formation of the leucogranite.

7.4. Intrusion of norite as causative agent of the anatectic event

The liquid-liquid contact relation between the norite and leucogranite, and their within error comparable ages, imply that intrusion of the norite caused anatexis of the diorite gneiss. This inference is substantiated by the preferred accumulation of leucocratic material along the contact between the diorite gneiss and the norite (see Figs. 4g and 5a, d, e). There is petrographic continuity between the

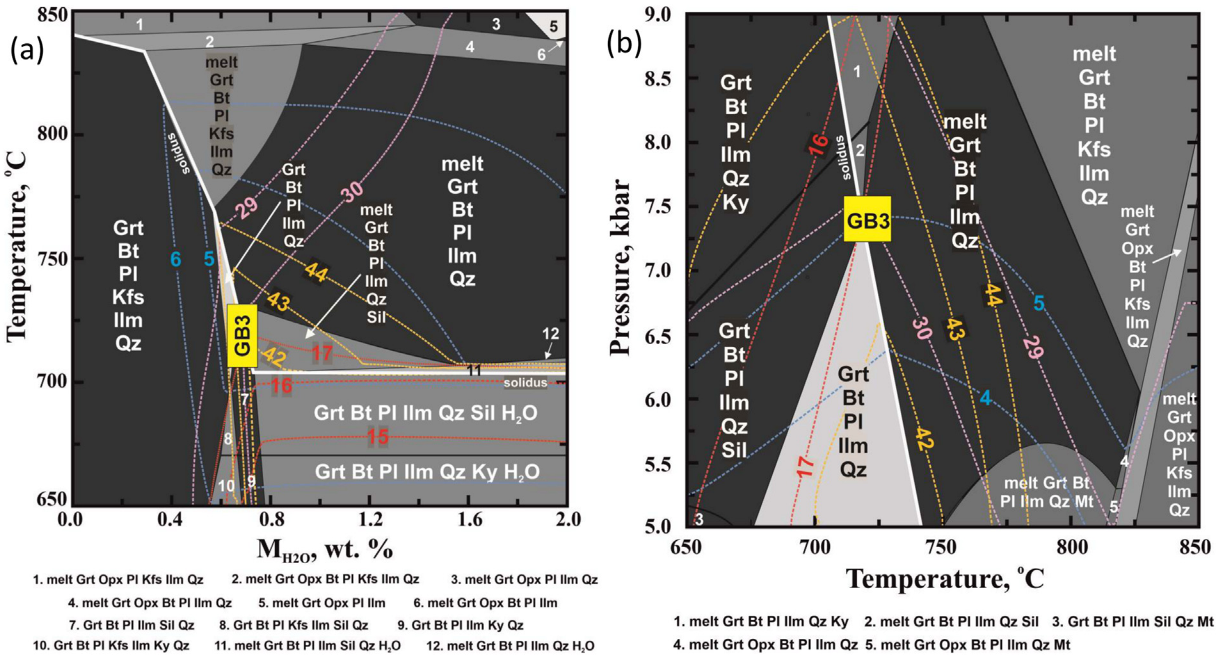

Fig. 13. (a) The T-M_{H2O} pseudosection for the composition of the diorite gneiss GB3 constructed for 7 kbar, showing major phase fields and selected isopleths of mineral compositions, corresponding to those in the sample: N_{Mg}^{Grt} (red), N_{Ca}^{Grt} (blue), N_{Mg}^{Bt} (yellow), N_{Ca}^{Pl} (magenta). Yellow box indicates the best region of isopleth convergence at M_{H2O} about 0.7 wt%. The region corresponds to the phase field melt + Grt + Bt + Pl + Ilm + Qz close to the solidus (white curved line). (b) The P-T pseudosection for the composition of the diorite gneiss GB3 constructed for a water content in the system of 0.7 wt%, showing major phase fields and selected isopleths of mineral compositions (colored dotted lines), corresponding to those in the sample: N_{Mg}^{Grt} (red), N_{Ca}^{Grt} (blue), N_{Mg}^{Bt} (yellow), N_{Ca}^{Pl} (magenta). Yellow box indicates the best region of isopleth convergence. The region corresponds to the phase field melt + Grt + Bt + Pl + Ilm + Qz close to the solidus (white curved line). (For interpretation of the references to colour in this figure legend, the reader is referred to the web version of this article.)

leucosomes in the diorite gneiss and the leucogranite bordering the norite on different scales (Figs. 4g and 5d), which points to a melt flow-accumulation network (e.g., Brown, 2004; Vanderhaeghe, 1999). This is comparable to cases where emplacement of mafic plutons has been argued to cause partial melting of mid-crustal rocks, with the resultant leucocratic material tending to collect adjacent to the intruded body (e.g., Barnes et al., 2002). Thus, the contact zone (in the present case between the diorite gneiss and norite) likely acted as an anisotropic boundary for the accumulation of granitic material.

7.5. Extending the foot print of Bushveld LIP

The possible aerial extent of the ~2.06–2.05 Ga Bushveld LIP is delineated by the low seismic velocity zone in the Kaapvaal cratonic mantle related to Bushveld magmatism (see dotted line in inset in Figs. 1 and 2; James and Fouch, 2002; Griffin et al., 2003; Richardson and Shirey, 2008; Rajesh et al., 2013a; Ernst, 2014). The Mahalapye Complex falls into this area and, therefore, within the possible extent of the Bushveld LIP (see inset in Figs. 1 and 2). Together with other diorite-bearing units, the ~2.06 Ga diorite gneiss from the Mahalapye Complex forms part of the Bushveld LIP (see Table 1 and Fig. 2; Rajesh et al., 2013a and references therein; Ernst, 2014). The ~2.05 Ga norite associated with the diorite gneiss is similar to marginal facies norites from the Bushveld Complex and the Molopo Farms Complex layered intrusions (Rajesh, 2019). The $^{207}Pb/^{206}Pb$ ages of xenocrystic zircons (2163 Ma, 2263 Ma, 2614 Ma, 2767 Ma, 2843 Ma; Figs. 10i to l, m; Table 3) obtained from the Mahalapye norite correlate with the peaks of distribution (~2.1 Ga, ~2.2 Ga, ~2.3–2.4 Ga, ~2.6 Ga, ~2.7 Ga, ~2.8 Ga, ~3.1 Ga) of detrital zircon ages from rocks of the Dominion Group, Ventersdorp Supergroup and Transvaal Supergroup (e.g., Beukes et al., 2019; Schröder et al., 2016; Zeh et al., 2016), which constitute the country rocks of the Bushveld Complex. Minor volumes of silicic rocks formed throughout the known age range of the Bushveld LIP (see Table 1 and Fig. 2). The age reported here (~2.051 Ga) corresponds to the younger limit of the period of silicic magmatism associated with the Bushveld LIP (see Table 1). In view of the relation between the syn-Bushveld (~2.054 Ga) norite dykes and sills and resulting ~2.051 Ga anatectic event, we argue that the leucogranites associated with diorite gneiss in the Mahalapye Complex were formed in response to emplacement of the Bushveld LIP.

7.6. Implications for overprint event(s) in high-grade terranes along Archean cratonic margins

Overprint event(s) in high-grade terranes can be widely preserved in different rocks (meta-supracrustal rocks, mafic-ultramafic rocks, granitoid gneisses). In comparison to their Archean cratonic counterparts, high-grade terranes at their borders are strongly reworked by various tectono-thermal events involving metamorphic, anatectic, and metasomatic processes. In most cases, the causative agent of the overprints in high-grade terranes is related to orogenic events of similar age. Peraluminous leucogranites that are related to orogenic events typically form massive bodies (e.g., Dey et al., 2014; Frost et al., 2016; Mikkola et al., 2012). Underplating by mafic magmas is another causative agent for anatexis and formation of leucogranites in high-grade terranes (e.g., Annen et al., 2006; Barnes et al., 2002). High-temperature magmatism often triggers extensive melting of the crust producing voluminous granitoid melts. In contrast, the studied leucogranite associated with diorite gneiss occurs as thin veins and dykes. Low melt content is supported by results of the phase equilibria modelling. Melting of crustal rocks by thermal input from intruding magmas depends on the temperature and volume of the intruding magma (Hersum et al., 2007; Holness et al., 2005). In comparison to the massive Bushveld Complex layered ultramafic-mafic intrusion, the norite dykes and sills that intruded the Mahalapye Complex are smaller in extent (Fig. 1). It resulted in small volume of leucogranite material. Relatively low temperatures of melting (~730 °C; Figs. 12 and 3b) is likely imposed by a lower temperature of intrusion. It is postulated that during passage through country rocks (as indicated by zircon xenocrysts; see Fig. 10i to l, m), norite intrusions lost their initial perceived high temperatures (compare position of northern limb of the Bushveld Complex with respect to the Mahalapye Complex in Fig. 3). The high content of assimilated quartz with lobate rounded grain margins in the norite supports this inference (Rajesh, 2019). Thus, direct intrusion of mafic magmas can be a possible causative agent for the metamorphic-anatectic overprint in high-grade terranes along cratonic margins. However, the extent of the related anatectic overprint and the resultant volume of the leucogranite is smaller. The processes/features that are illustrated in the present study are likely characteristic of 'failed' pluton development where the melt fraction is below a critical value >30%, which is sufficient for a melt to leave the source (e.g., Brown, 2004).

As the norites form part the Bushveld LIP, it is worth delineating the footprint of this large intracratonic event. Syn-Bushveld intrusions occur within the Southern Marginal Zone of the Limpopo Complex, which is another high-grade terrane occurring along the north-eastern margin of the Kaapvaal Craton (see Fig. 3). They include the 2.06–2.05 Ga Schiel alkaline complex (Graupner et al., 2018; Laurent and Zeh, 2015; Walraven et al., 1992), and 2.06–2.05 Ga mafic-ultramafic rocks [2059 ± 3 Ma, 2053 ± 5 Ma (U–Pb zircon; Huthmann et al., 2016)], which are considered as an extension of the northern limb of the Bushveld Complex (see Figs. 2 and 3). Paleoproterozoic overprint events in the Southern Marginal Zone are grouped into two episodes: ~2.06–2.05 Ga and ~ 2.04–1.95 Ga (Barton Jr. and Van Reenen, 1992; Belyanin et al., 2014; Rajesh et al., 2014b, 2020a). The ~2.06–2.05 Ga episode is related to the Bushveld magmatic event. The younger episode correlates with the metasomatic overprint and reactivation along shear zones (see Rajesh et al., 2020a). Significantly, the Paleoproterozoic overprint ages reported from the rest of the Limpopo Complex high-grade terrane are either ~2.04 Ga or younger (e.g., Boshoff et al., 2006; Buick et al., 2007; Chudy et al., 2008; Holzer et al., 1999; Jaeckel et al., 1997; Kamber et al., 1995; Rajesh et al., 2014a). The ~2.06–2.05 Ga overprint ages are not reported from these terranes which are away from the cratonic margin. It seems that the overprint events related to the Bushveld magmatic event are restricted to high-grade terranes immediately adjacent to the cratonic margin. This places constraints on the extent of the Precambrian LIP magmatism and related overprint.

Supplementary data to this article can be found online at https://doi.org/10.1016/j.lithos.2020.105805.

Declaration of Competing Interest

The authors declare that they have no known competing financial interests or personal relationships that could have appeared to influence the work reported in this paper.

Acknowledgements

Branko Corner and Terence (Spike) McCarthy are thanked for giving permission to use the TMI image of southern Africa as a base map in Fig. 1. University of Johannesburg (UJ) and Botswana International University of Science and Technology (BIUST) are thanked for facilities. Daniel Harlov, Stefan Jung and anonymous are thanked for detailed constructive comments which helped in streamlining the contents of the study. Xian Hua Li is thanked for efficient editorial handling. A number of postgraduate and undergraduate students at BIUST helped with field work sessions covering the different corners of Mahalapye Complex. Particular mention goes to Thembiso Basupi, Mpho Keeditse, Jacob Kaavera and Thuto Mokatse. The LA-MC-ICPMS and Q-ICPMS equipments housed in the Department of Geology, UJ, have respectively been funded by NRF-NEP grant #93208 and DST-NRF CIMERA. This study was partially supported by the Russian Scientific Foundation (project no. 18-17-00206 to OGS), the Research Program AAAA-A18-118020590148-3 of the Korzhinskii Institute of Experimental Mineralogy RAS, and the Department of Science and Technology – National Research Foundation (DST-NRF CIMERA).

References

Abdel-Rahman, A.M., 1994. Nature of biotite from alkaline, calc-alkaline and peraluminous magmas. J. Petrol. 35, 525–541.
Annen, C., Blundy, J.D., Sparks, R.S.J., 2006. The genesis of intermediate and silicic magmas in deep crustal hot zones. J. Petrol. 47, 505–539.
Barnes, C.G., Yoshinobu, A.S., Prestvik, T., Nordgulen, O., Karlsoon, H.R., Sundvoll, B., 2002. Mafic magma intraplating: Anatexis and hydridization in arc crust, Bindal batholith, Norway. J. Petrol. 43, 2171–2190.
Barton Jr., J.M., Van Reenen, D.D., 1992. The significance of Rb-Sr ages of biotite and phlogopite for the thermal history of the Central and Southern Marginal Zones of the Limpopo Belt of southern Africa and the adjacent portions of the Kaapvaal Craton. Precambrian Res. 55, 17–31.
Belyanin, G.A., Kramers, J.D., Vorster, C., Knoper, M.D., 2014. The timing of successive fluid events in the Southern Marginal Zone of the Limpopo Complex, South Africa: Constraints from 40Ar-39Ar geochronology. Precambrian Res. 254, 169–193.
Berman, R.G., 1988. Internally-Consistent Thermodynamic Data for Minerals in the System Na_2O-K_2O-CaO-MgO-FeO-Fe_2O_3-Al_2O_3-SiO_2-TiO_2-H_2O-CO_2. J. Petrol. 29, 445–522.
Berman, R.G., 2007. WinTWQ (version 2.3): A software package for performing internally-consistent thermobarometric calculations. Geological Survey of Canada Open File, p. 5462.
Berman, R.G., Aranovich, L.Ya., 1996. Optimized standard state and solution properties of minerals I model calibration for olivine, orthopyroxene, cordierite, garnet, and ilmenite in the system FeO-MgO-CaO-Al_2O_3-TiO_2-SiO_2. Contribution to Mineralogy and Petrology 126, 1–24.
Beukes, N.J., De Kock, M.O., Vorster, C., Ravhura, L.G., Frei, D., Gumsley, A.P., Harris, C., 2019. The age and country rock provenance of the Molopo Farms Complex: implications for Transvaal Supergroup correlation in southern Africa. South African Journal of Geology 122 (1), 39–56.
Boshoff, R., van Reenen, D.D., Smit, C.A., Perchuk, L.L., Kramers, J.D., Armstrong, R., 2006. Geologic history of the central zone of the Limpopo complex: the West Alldays area. J. Geol. 114, 699–716.
Brown, M., 2004. Melt extraction from lower continental crust. Transactions of the Royal Society of Edinburgh–Earth Sciences 95, 35–48.
Buick, I.S., Hermann, J., Roland, M., Gibson, R.L., 2007. The timing of sub-solidus hydrothermal alteration in the Central Zone, Limpopo Belt (South Africa): constraints from titanite U–Pb geochronology and REE partitioning. Lithos 98, 97–117.
Carney, J.N., Aldiss, D.T., Lock, N.P., 1994. The Geology of Botswana. Bulletin Geological Survey, Botswana 37 (113 pp.).
Chavagnac, V., Kramers, J.D., Naegler, T.F., Holzer, L., 2001. The behaviour of Nd and Pb isotopes during 2·0 Ga migmatization in paragneisses of the Central Zone of the Limpopo Belt (South Africa and Botswana). Precambrian Res. 112, 51–86.
Chudy, T.C., Zeh, A., Gerdes, A., Klemd, R., Barton Jr., J.M., 2008. Palaeoarchaean (3.3 Ga) mafic magmatism and Palaeoproterozoic (2.02 Ga) amphibolite-facies metamorphism in the Central Zone of the Limpopo Belt: new geochronological, petrological and geochemical constraints from metabasic and metapelitic rocks from the Venetia area. South African Journal of Geology 111, 387–408.
Dey, S., Nandy, J., Choudhary, A.K., Liu, Y., Zong, K., 2014. Origin and evolution of granitoids associated with the Kadiri greenstone belt, eastern Dharwar craton: a history of orogenic to anorogenic magmatism. Precambrian Res. 246, 64–90.
Engelbrecht, J.P., 1990. Contact metamorphic processes related to the aureole of the Bushveld Complex in the Marico District, western Transvaal, South Africa. South African Journal of Geology 93, 339–349.
Ermanovics, I.F., 1980. The geology of the Mokgware hills area (an Explanation of quarter degree sheet 2226D). Bulletin of Geological Survey, Botswana 13, 1–86.
Ernst, R., 2014. Large Igneous Provinces. Cambridge University Press (653 pp.).
Frost, B.R., Arculus, R.J., Barnes, C.G., Collins, W.J., Ellis, D.J., Frost, C.D., 2001. A geochemical classification of granitic rocks. J. Petrol. 42, 2033–2048.
Frost, C.D., Swapp, S.M., Frost, B.R., Finley-Blasi, L., Fitz-Gerald, D.B., 2016. Leucogranites of the Teton Range, Wyoming: a record of Archean collisional orogeny. Geochim. Cosmochim. Acta 185, 528–549.
Graupner, T., Klemd, R., Henjes-Kunst, F., Goldmann, S., Behnsen, H., Gerdes, A., Dohrmann, R., Barton Jr., J.M., Opperman, R., 2018. Formation conditions and REY enrichment of the 2060 Ma phosphorus mineralization at Schiel (South Africa): geochemical and geochronological constraints. Miner. Deposita 53 (l8), 1117–1142.
Griffin, W.L., O'Reilly, S.Y., Natapov, L.M., Ryan, C.G., 2003. The evolution of lithospheric mantle beneath the Kalahari Craton and its margins. Lithos 71, 215–241.
Harangi, S.Z., Downes, H., Kósa, L., Szabó, C., Thirlwall, M.F., Mason, P.R.D., Mattey, D., 2001. Almandine garnet in calc-alkaline volcanic rocks of the northern Pannonian basin (Eastern-Central Europe): Geochemistry, petrogenesis and geodynamic implications. J. Petrol. 42, 1813–1843.
Harlov, D.E., Marschall, H.R., Hanel, M., 2007. Fluorapatite-monazite relationships in granulite-facies metapelites, Schwarzwald, southwest Germany. Mineralogical Magazine 71 (2), 223–234.
Harris, N., McMillan, A., Holness, M., Uken, R., Watkeys, M., Rogers, N., Fallick, A., 2003. Melt generation and fluid flow in the thermal aureole of the Bushveld Complex. J. Petrol. 44, 1031–1054.

Hersum, T.G., Marsh, B.D., Simon, A.C., 2007. Contact partial melting of granitic country rock, melt segregation, and re-injection as dikes into Ferrar Dolerite Sills, McMurdo Dry Valleys, Antarctica. J. Petrol. 48, 2125–2148.
Hisada, K., Paya, B.K., Van Reenen, D.D., 2000. Partial melting of pelitic rocks in the Mahalapye Plutonic Block, eastern Botswana: evidence for 2 Ga low-P–high-T migmatization in the Limpopo Granulite Complex. Petrology 8, 19–37.
Hisada, K., Perchuk, L.L., Gerya, T.V., Van Reenen, D.D., Paya, B.K., 2005. P-T-fluid evolution in the Mahalapye Complex, Limpopo high-grade terrane, eastern Botswana. J. Metam. Geol. 23, 313–334.
Holness, M.B., Dane, K., Sides, R., Richardson, C., Caddick, M., 2005. Melting and melt segregation in the aureole of the Glenmore Plug, Ardnamurchan. J. Metam. Geol. 23, 29–43.
Holzer, L., Barton Jr., J.M., Paya, B.K., Kramers, J.D., 1999. Tectonothermal history in the western part of the Limpopo Belt: test of tectonic models and new perspectives. Journal of African Earth Sciences 28, 383–402.
Hoskin, P.W.O., Black, L.P., 2000. Metamorphic zircon formation by solid-state recrystallization of protolith igneous zircon. J. Metam. Geol. 18, 423–439.
Huthmann, F.M., Yudovskaya, M.A., Frei, D., Kinnaird, J.A., 2016. Geochronological evidence for an extension of the Northern Lobe of the Bushveld Complex, Limpopo Province, South Africa. Precambrian Res. 280, 61–75.
Jaeckel, P., Kröner, A., Kamo, S.L., Brandl, G., Wendt, J.I., 1997. Late Archaean to early Proterozoic granitoid magmatism and high grade metamorphism in the central Limpopo belt, South Africa. Journal of the Geological Society of London 154, 25–44.
James, D.E., Fouch, M., 2002. Formation and evolution of Archaean cratons: insights from southern Africa. In: Fowler, C.M.R., Ebinger, C.J., Hawkesworth, C.J. (Eds.), The Early Earth: Physical, Chemical and Biological Development. Geological Society, London, Special Publications. 199, pp. 1–26.
Johnson, T.E., Gibson, R.L., Brown, M., Buick, I.S., Cartwright, I., 2003. Partial melting of metapelitic rocks beneath the Bushveld Complex, South Africa. J. Petrol. 44, 789–813.
Jung, S., Hoernes, S., Mezger, K., 2000. Geochronology and petrology of migmatites from the Proterozoic Damara Belt — importance of episodic fluid-present disequilibrium melting and consequences for granite petrology. Lithos 51, 153–179.
Kaavera, J., Rajesh, H.M., Tsunogae, T., Belyanin, G.A., 2018. Marginal facies and compositional equivalents of Bushveld parental sills from the Molopo Farms complex layered intrusion, Botswana: petrogenetic and mineralization implications. Ore Geol. Rev. 92, 506–528.
Kamber, B.S., Kramers, J.D., Napier, R., Cliff, R.A., Rollinson, H.R., 1995. The Triangle Shear zone, Zimbabwe, revisited: new data document an important event at 2.0 Ga in the Limpopo Belt. Precambrian Res. 70, 191–213.
Kaneko, Y., Miyano, T., 1990. Contact metamorphism by the Bushveld Complex in the northeastern Transvaal, South Africa. J. Mineral. Petrol. Econ. Geol. 85, 66–81 (in Japanese with English abstract).
Key, R.M., 1979. The geology of the country around Machaneng and Chadibe (an explanation of quarter degree sheets 2327A and 2327B). Bulletin of Geological Survey, Botswana 15, 1–72.
Kramers, J.D., Frei, R., Newville, M., Kober, B., Villa, I.M., 2009. On the valency state of radiogenic lead in zircon and its consequences. Chem. Geol. 261, 3–10.
Laurent, O., Zeh, A., 2015. A linear Hf isotope-age array despite different granitoid sources and complex Archean geodynamics: example from the Pietersburg block (South Africa). Earth Planet. Sci. Lett. 430, 326–338.
Maier, W.D., Barnes, S.J., Groves, D.I., 2013. The Bushveld Complex, South Africa: formation of platinum–palladium, chrome-and vanadium-rich layers via hydrodynamic sorting of a mobilized cumulate slurry in a large, relatively slowly cooling, subsiding magma chamber. Miner. Deposita 48 (1), 1–56.
McCarthy, T.S., Corner, B., Lombard, H., Beukes, N.J., Armstrong, R.A., Cawthorn, R.G., 2018. The pre-Karoo geology of the southern portion of the Kaapvaal Craton, South Africa. South African Journal of Geology 121 (1), 1–22.
McCourt, S., Armstrong, R.A., 1998. SHRIMP U-Pb zircon geochronology of granites from the Central Zone, Limpopo Belt, southern Africa: implications for the age of the Limpopo Orogeny. South African Journal of Geology 101, 329–338.
McCourt, S., Kampunzu, A.B., Bagai, Z., Armstrong, R.A., 2004. Crustal architecture of Archaean terranes in Northeastern Botswana. South African Journal of Geology 107, 146–158.
Mikkola, P., Lauri, L.S., Käpyaho, A., 2012. Neoarchean leucogranitoids of the Kianta Complex Karelian Province, Finland: source characteristics and processes responsible for the observed heterogeneity. Precambrian Res. 206–207, 72–86.
Millonig, L.J., Zeh, A., Gerdes, A., Klemd, R., Barton Jr., J.M., 2010. Decompressional heating of the Mahalapye Complex Limpopo Belt, Botswana: a response to Palaeoproterozoic magmatic underplating? J. Petrol. 51, 703–729.
Montel, J.M., Vielzeuf, D., 1997. Partial melting of metagreywackes, Part II. Compositions of minerals and melts. Contributions to Mineralogy and Petrology 128, 176–196.
Mungall, J.E., Kamo, S.L., McQuade, S., 2016. U–Pb geochronology documents out-of-sequence emplacement of ultramafic layers in the Bushveld Igneous Complex of South Africa. Nat. Commun. 7, 13385.
Nell, J., 1985. The Bushveld metamorphic aureole in the Potgietersrus area: evidence for a two-stage metamorphic event. Econ. Geol. 80, 1129–1152.
Patiño Douce, A.E., 1999. What do experiments tell us about the relative contributions of crust and mantle to the origin of granitic magmas? In: Castro, A., Fernandez, C., Vigneresse, J.L. (Eds.), Understanding granites. Integrating New and Classical Techniques. 158, pp. 55–75 Journal of the Geological Society, Special Publication
Patiño Douce, A.E., Beard, J.S., 1996. Effects on P, f(O_2) and Mg/Fe ratio on dehydration melting of model metagreywackes. J. Petrol. 37, 999–1024.
Pidgeon, R.T., 1992. Recrystallisation of oscillatory zoned zircon: some geochronological and petrological implications. Contrib. Mineral. Petrol. 110, 463–472.
Rajesh, H.M., 2019. Norite from the Mahalapye granitoid complex, northern edge of Kaapvaal Craton: Implications for the extent of the Paleoproterozoic Bushveld LIP. Precambrian Res. 324, 146–154.
Rajesh, H.M., Chisonga, B.C., Shindo, K., Beukes, N.J., Armstrong, R.A., 2013a. Petrographic, geochemical and SHRIMP U-Pb titanite age characterization of the Thabazimbi mafic sills: Extended time frame and a unifying petrogenetic model for the Bushveld Large Igneous Province. Precambrian Res. 230, 79–102.
Rajesh, H.M., Belyanin, G.A., Safonov, O.G., Kovaleva, E.I., Golunova, M.A., van Reenen, D.D., 2013b. Fluid-induced dehydration of the Paleoarchean Sand River biotite-hornblende gneiss, Central Zone, Limpopo Complex, South Africa. J. Petrol. 54, 41–74.
Rajesh, H.M., Safonov, O.G., Belyanin, G.A., Kramers, J.D., 2014a. Monazite-fluorapatite characteristics as evidence for interplay between ~2.04 Ga fluid-induced dehydration and melting of the Sand River Gneiss, Limpopo Complex, South Africa. South African Journal of Geology 117, 237–254.
Rajesh, H.M., Santosh, M., Wan, Y., Liu, S.J., Belyanin, G.A., 2014b. Ultrahigh temperature granulites and magnesium charnockites: evidence for Neoarchean accretion along the northern margin of the Kaapvaal Craton. Precambrian Res. 246, 150–159.
Rajesh, H.M., Liu, S.J., Wan, Y., 2020a. Mesoarchean TTG magmatism from the northeastern margin of the Kaapvaal Craton, southern Africa: Arguments for an exotic terrane (remnant of Pilbara Craton?). Precambrian Res. 337, 105552.
Rajesh, H.M., Mokatse, T., Wan, Y., 2020b. Complexity of characterizing mafic-ultramafic remnants of Archean layered complexes in high-grade terranes: the scenario from Motloutse complex, southwestern Zimbabwe craton. Lithos 352-353, 105255.
Richardson, S.H., Shirey, S.B., 2008. Continental mantle signature of Bushveld magmas and coeval diamonds. Nature 453, 910–913.
Safonov, O.G., Kovaleva, E.I., Kosova, S.A., Rajesh, H.M., Belyanin, G.A., Golunova, M.A., Van Reenen, D.D., 2012. Experimental and petrological constraints on local-scale interaction of biotite-amphibole gneiss with H_2O-CO_2-(K, Na)Cl fluids at middle-crustal conditions: example from the Limpopo Complex, South Africa. Geoscience Frontiers 3, 829–841.
Sawyer, E.W., 1999. Criteria for the recognition of partial melting. Physics and Chemistry of the Earth, Series A 24, 269–279.
Schröder, S.N., Beukes, N.J., Armstrong, R.A., 2016. Detrital zircon constraints on the tectonostratigraphy of the Paleoproterozoic Pretoria Group, South Africa. Precambrian Res. 278, 362–393.
Scoates, J.S., Friedman, R.M., 2008. Precise age of the platiniferous Merensky Reef, Bushveld complex, South Africa, by the U-Pb zircon chemical abrasion ID-TIMS technique. Econ. Geol. 103 (3), 465–471.
Scoates, J.S., Wall, C.J., Friedman, R.M., VanTongeren, J.A., Mathez, E.A., 2012. Age of the Bushveld Complex. Goldschmidt 2012 Conference Abstracts, 22nd V.M. Goldschmidt Conference "Earth in Evolution" June 24–29, 2012, Montreal, Quebec, Canada. p. 2348.
Skinner, A.C., 1978. The geology of the Mahalapye area (an explanation of quarter degree sheet 2326B). Bulletin of the Geological Survey, Botswana 9, 1–60.
Sun, S.-S., McDonough, W.F., 1989. Chemical and isotopic systematics of oceanic basalts: implications for mantle composition and processes. In: Saunders, A.D., Norry, M.J. (Eds.), Magmatism in Ocean Basins. Geological Society of London Special Publication, pp. 313–345.
Vanderhaeghe, O., 1999. Pervasive melt migration from migmatites to leucogranite in the Shuswap metamorphic core complex, Canada: control of regional deformation. Tectonophysics 312, 35–55.
Vielzeuf, D., Montel, J.M., 1994. Partial melting of metagreywackes. Part I. Fluid-absent experiments and phase relationships. Contributions to Mineralogy and Petrology 117, 375–393.
Wabo, H., Olsson, J.R., De Kock, M.O., Humbert, F., Soderlund, U., Klausen, M., 2016. New U-Pb age and paleomagnetic constraints from the Uitkomst Complex. South Africa: clues to the timing of intrusion. GFF 138, 152–163.
Walraven, F., Frick, C., Lubala, R.T., 1992. Pb-isotope geochronology of the Schiel Complex, Northern Transvaal, South Africa. Journal of African Earth Sciences 15 (1), 103–110.
Waters, D.J., Lovegrove, D.P., 2002. Assessing the extent of disequilibrium and overstepping of prograde metamorphic reactions in metapelites from the Bushveld Complex aureole, South Africa. J. Metam. Geol. 20, 135–149.
Wolf, M.B., London, D., 1995. Incongruent dissolution of REE- and Sr-rich apatite in peraluminous granitic liquids: differential apatite, monazite and xenotime solubilities during anatexis. Am. Mineral. 80, 765–775.
Zeh, A., Gerdes, A., Klemd, R., Barton Jr., J.M., 2007. Archaean to Proterozoic crustal evolution in the Central Zone of the Limpopo Belt South Africa/Botswana: constraints from combined U–Pb and Lu–Hf isotope analyses of zircon. J. Petrol. 48, 1605–1639.
Zeh, A., Ovtacharova, M., Wilson, A.H., Schaltegger, U., 2015. The Bushveld Complex was emplaced and cooled in less than one million years - results of zirconology, and geotectonic implications. Earth Planet. Sci. Lett. 418, 103–114.
Zeh, A., Wilson, A., Ovtcharova, M., 2016. Source and age of Upper Transvaal Supergroup, South Africa: Age-Hf isotope record of zircons in Magaliesberg quartzite and Dullstroom lava, and implications for Paleoproterozoic (2.5–2.0 Ga) continent reconstruction. Precambrian Res. 278, 1–21.